



# 1 Phase state and viscosity of secondary organic aerosols over China 2 simulated by WRF-Chem

3 Zhiqiang Zhang<sup>1,2</sup>, Ying Li<sup>1</sup>, Haiyan Ran<sup>1,2</sup>, Junling An<sup>1</sup>, Yu Qu<sup>1</sup>, Wei Zhou<sup>1</sup>, Weiqi Xu<sup>1</sup>, Weiwei Hu<sup>3</sup>,  
4 Hongbin Xie<sup>4</sup>, Zifa Wang<sup>1</sup>, Yele Sun<sup>1</sup>, Manabu Shiraiwa<sup>5</sup>

5 <sup>1</sup>State Key Laboratory of Atmospheric Boundary Layer Physics and Atmospheric Chemistry, Institute of Atmospheric Physics,  
6 Chinese Academy of Sciences, Beijing 100029, China

7 <sup>2</sup>College of Earth and Planetary Sciences, University of Chinese Academy of Sciences, Beijing 100049, China

8 <sup>3</sup>State Key Laboratory of Organic Geochemistry, Guangzhou Institute of Geochemistry, Chinese Academy of Sciences,  
9 Guangzhou 510640, China

10 <sup>4</sup>Key Laboratory of Industrial Ecology and Environmental Engineering (Ministry of Education), School of Environmental  
11 Science and Technology, Dalian University of Technology, Dalian 116024, China

12 <sup>5</sup>Department of Chemistry, University of California, Irvine, CA 92697-2025, USA

13 *Correspondence to:* Ying Li (liying-iap@mail.iap.ac.cn)

14 **Abstract.** Secondary organic aerosols (SOA) can exist in liquid, semi-solid or amorphous solid states, which are rarely  
15 accounted for in current chemical transport models (CTMs). Missing the information of SOA phase state and viscosity in  
16 CTMs impedes accurate representation of SOA formation and evolution, affecting the predictions of aerosol effects on air  
17 quality and climate. We have previously developed a method to estimate the glass transition temperature ( $T_g$ ) of an organic  
18 compound based on volatility. In this study, we apply this method to predict the phase state and viscosity of SOA particles  
19 over China in summer of 2018 using the Weather Research and Forecasting model coupled to Chemistry (WRF-Chem). This  
20 is the first time that spatial distributions of the SOA phase state over China are investigated by a regional CTM. Simulations  
21 show that  $T_g$  values of dry SOA range from ~287 K to 305 K, with higher values in the northwestern China where SOA  
22 particles have larger mass fractions of low volatility compounds. Considering water uptake by SOA particles, the SOA  
23 viscosity also shows a prominent geospatial gradient that highly viscous or solid SOA particles are mainly found in the  
24 northwestern China. The lowest and highest SOA viscosity values both occur over the Qinghai-Tibet Plateau that the solid  
25 phase state is predicted over dry and high-altitude areas and the liquid phase state is predicted mainly in the south of the  
26 plateau with high relative humidity during the summer monsoon season. The characteristic mixing timescale of organic  
27 molecules in 200 nm SOA particles is calculated based on the simulated particle viscosity and the bulk diffusion coefficient  
28 of organic molecules. Calculations show that during the simulated period the percent time of the mixing timescale longer  
29 than 1 h is  $> 70\%$  at the surface and at 500 hPa in most areas of the northern China, indicating that kinetic partitioning  
30 considering the bulk diffusion in viscous particles may be required for more accurate prediction of SOA mass concentrations  
31 and size distributions over these areas. Sensitivity simulations show that including the formation of extremely low-volatile  
32 organic compounds, the percent time that a SOA particle is in the liquid phase state decreases by up to 12 % in the



33 southeastern China during the simulated period. With an assumption that the organic and inorganic compounds are always  
34 internally mixed in one phase, we show that the water absorbed by inorganic species can significantly lower the simulated  
35 viscosity over the southeastern China. This indicates that constraining the uncertainties in simulated SOA volatility  
36 distributions and accurately predicting the occurrence of phase separation would improve prediction of viscosity in  
37 multicomponent particles in southeastern China.

## 38 **1 Introduction**

39 Secondary organic aerosols (SOA) are major components of atmospheric fine particles, impacting air quality, climate and  
40 public health (Jimenez et al., 2009; Pöschl and Shiraiwa, 2015). The formation and evolution of SOA involve both chemical  
41 reactions and mass transport in the gas and particle phases (Ziemann and Atkinson, 2012). This complexity makes accurate  
42 representation of SOA evolution in chemical transport models (CTMs) challenging, leading to a large uncertainty in  
43 evaluating SOA impacts on air quality and climate (Kanakidou et al., 2005; Shrivastava et al., 2017).

44 Current CTMs usually assume that SOA particles are homogeneous and well-mixed liquids, with rapid establishment of  
45 gas-particle equilibrium applied in simulations of SOA formation and partitioning (Pankow, 1994; Donahue et al., 2006). It  
46 has been shown that SOA can exist in liquid (low dynamic viscosity  $\eta$ ,  $\eta < 10^2$  Pa s), semi-solid ( $10^2$  Pa s  $\leq \eta \leq 10^{12}$  Pa s) or  
47 solid (amorphous or glassy solid;  $\eta > 10^{12}$  Pa s) states, depending on particle chemical composition and atmospheric  
48 conditions, such as ambient temperature ( $T$ ) and relative humidity (RH) (Koop et al., 2011; Reid et al., 2018). Viscosities can  
49 be converted to bulk diffusion coefficients via the Stokes-Einstein equation (Einstein, 1905; Seinfeld and Pandis, 2016) or  
50 the fractional Stokes-Einstein equation (Price et al., 2016; Evoy et al., 2019; Evoy et al., 2020). The phase state, viscosity,  
51 and bulk diffusivity of SOA are important in many aerosol processes. The semi-solid or solid phase state can prolong the  
52 equilibration timescales in the gas-particle partitioning, indicating a need of considering kinetic limitations in the SOA  
53 partitioning into highly viscous particles (Shiraiwa and Seinfeld, 2012; Roldin et al., 2014; Zaveri et al., 2014; Li and  
54 Shiraiwa, 2019). The viscosity of SOA can impact the rates of heterogeneous and multiphase reactions (Marshall et al., 2018;  
55 Zhang et al., 2019a), photochemistry (Liu et al., 2018; Dalton and Nizkorodov, 2021; Baboosian et al., 2022), and the  
56 uptake of gaseous pollutants (e.g., O<sub>3</sub>, OH, N<sub>2</sub>O<sub>5</sub>, NO<sub>2</sub>, NH<sub>3</sub>, and SO<sub>2</sub>) and water vapor (Abbatt et al., 2012; Kuwata and  
57 Martin, 2012; Preston and Zuend, 2022), with implications for accurate predictions of atmospheric chemical composition  
58 (Reid et al., 2018). The SOA phase state also affects particle size distribution evolution (Shiraiwa et al., 2013; Zaveri et al.,  
59 2018) and ice nucleation pathways (Knopf and Alpert, 2023).

60 Accurate predictions of the viscosity need the information of molecular structures and functional groups (Song et al.,  
61 2016; Rothfuss and Petters, 2017; Gervasi et al., 2020; Galeazzo and Shiraiwa, 2022); however, molecular specificity is  
62 often difficult to be obtained in ambient measurements. Currently there are only a few methods developed to predict the



63 phase state of ambient SOA particles, and successfully be implemented in CTMs. Li, Shiraiwa and coauthors first developed  
64 a parameterization predicting the glass transition temperature ( $T_g$ ) based on the molar mass ( $M$ ) and the atomic O/C ratio for  
65 carbon-hydrogen (CH) and carbon-hydrogen-oxygen (CHO) compounds with their molar mass less than  $450 \text{ g mol}^{-1}$   
66 (Shiraiwa et al., 2017).  $T_g$  characterizes the temperature at which a phase transition between amorphous solid and semi-solid  
67 states occurs (Koop et al., 2011). When the ambient  $T$  is higher than  $T_g$ , a SOA particle is in a semi-solid or liquid phase state;  
68 otherwise, it behaves as an amorphous solid. This parameterization has been successfully coupled into CTMs simulating the  
69 SOA phase state over the globe (Shiraiwa et al., 2017) or the U.S. (Schmedding et al., 2020; Li et al., 2021b), showing that  
70 semi-solid and amorphous solid phase states frequently occurred in ambient SOA particles over dry lands or in the upper  
71 troposphere. Further parameterizations were developed to predict  $T_g$  as a function of the saturation mass concentration ( $C^0$ )  
72 and the O/C ratio of organic compounds, or as a function of  $C^0$  solely, which indirectly included the molecular structure  
73 effect on viscosity estimations (Li et al., 2020). This parameterization was added into the Weather Research and Forecasting  
74 Model coupled to chemistry (WRF-Chem) (Grell et al., 2005; Fast et al., 2006), and the simulations showed that the  
75 viscosity of SOA particles could be reasonably predicted during the dry-to-wet transition season in the Amazon rainforest  
76 (Rasool et al., 2021). Instead of predicting  $T_g$ , Maclean et al. developed parameterizations for viscosity as a function of  $T$  and  
77 RH based on measured viscosity data of laboratory SOA, and applied the viscosity parameterizations in CTMs to predict the  
78 mixing timescales of organic molecules and water molecules within SOA particles (Maclean et al., 2017; Maclean et al.,  
79 2021).

80 Investigations in the particle phase state over China are currently focused on field observations and laboratory  
81 experiments. Bounce factor measurements showed that submicrometer particles can be semi-solid in clear days and liquid in  
82 hazy days in Beijing, China (Liu et al., 2017). The phase state of  $\text{PM}_{2.5}$  (particulate matter with an aerodynamic diameter  $\leq$   
83  $2.5 \mu\text{m}$ ) was found to be mostly semisolid to solid in winter Beijing based on the measurements using optical microscopy  
84 combined with the poke-and-flow technique (Song et al., 2022). The RH-dependent viscosity of the proxies of actual  
85 ambient particles in Beijing was also investigated based on dual optical tweezers (Tong et al., 2022). The phase state of  
86 submicrometer particles in Beijing was retrieved from a polarization lidar that has the potential to infer the vertical profiles  
87 of phase state (Tan et al., 2020). The phase state of traffic-related secondary aerosols in Beijing may have a distinguished  
88 diurnal variation (Meng et al., 2021). The biomass burning aerosols, collected near a farmland in Yangtze River Delta, China,  
89 were found to exist in the non-solid phase state at relatively dry conditions (Liu et al., 2021b).

90 These measurements indicate that the particle phase state over China is highly variable under different atmospheric  
91 conditions. It is important to know the spatial distributions and time variations of the SOA phase state and viscosity in  
92 multicomponent particles to better quantify the aerosol effects on air quality, which, however, has not been investigated over  
93 China with air quality models on a regional scale. Here we use the WRF-Chem model simulated SOA volatility distributions  
94 to estimate the glass transition temperature and viscosity of SOA particles over China based on the parameterizations



95 developed in Li et al. (2020). We further calculate the diffusion coefficients and mixing timescales of organic molecules  
96 within SOA, which has implications in how to properly treat the SOA partitioning (instantaneous equilibrium vs. kinetic  
97 partitioning) in CTMs. As volatility and viscosity are closely related, we conduct a sensitivity calculation to evaluate the  
98 effects of the simulated SOA volatility distributions on viscosity estimations. We also conduct a sensitivity calculation to  
99 investigate how the water absorbed by inorganic components in PM<sub>2.5</sub> affects viscosity estimations, which has implications  
100 in predicting the viscosity of internally mixed ambient particles.

## 101 2 Methods

### 102 2.1 WRF-Chem model configuration

103 We use the WRF-Chem model version 3.7.1 (Grell et al., 2005; Fast et al., 2006) and simulate the period from 20 May to 23  
104 June 2018 with a spin-up period of 7 days (May 13 – 19). The meteorological initial and boundary conditions are from the  
105 National Centers for Environmental Prediction (NCEP) Global Forecast System (GFS) final (FNL) reanalysis data. The  
106 outputs of a global chemical transport model MOZART-4 (Emmons et al., 2010) provide initial and boundary conditions of  
107 chemical species over the outer domain. Anthropogenic emissions are from the MIX 2010 inventory for Asia (Li et al., 2017)  
108 and the MEIC 2016 inventory for China (<http://meicmodel.org.cn>) (Zheng et al., 2018). Biogenic emissions are calculated  
109 from the Model of Emissions of Gases and Aerosols from Nature (MEGAN2.1) (Guenther et al., 2012). We set up two  
110 domains (Fig. S1) with the horizontal resolutions of 81 km and 27 km, respectively, and 18 vertical layers are applied from  
111 the surface up to 100 hPa.

112 The utilized physical and chemical schemes are given in Table S1. We use the MOZART-4 mechanism (Emmons et al.,  
113 2010) for the gas-phase chemistry. The MOSAIC (Model for Simulating Aerosol Interactions and Chemistry) aerosol module  
114 (Zaveri et al., 2008) is applied for the aerosol chemistry and we represent aerosol particles with 4-size sections having dry  
115 diameters ranging from 39 nm to 10 μm (Knote et al., 2015). SOA formation is treated with the 1-D volatility basis set (VBS)  
116 approach (Donahue et al., 2006) which has been implemented into the MOSAIC aerosol module (Lane et al., 2008b;  
117 Ahmadov et al., 2012). Five volatility bins are considered (effective saturation mass concentrations  $C^*$  of  $10^{-4}$ , 1, 10, 100,  
118 and 1000 μg m<sup>-3</sup> at 298 K) in the official version 3.7.1 of the WRF-Chem model, with the enthalpy of vaporization ( $\Delta H_{\text{vap}}$ )  
119 values of 40, 131, 120, 109, and 98 kJ mol<sup>-1</sup> used in each volatility bin (Knote et al., 2015). We follow Knote et al. (2015)  
120 with SOA mass yields adopted for four volatility bins (1, 10, 100, and 1000 μg m<sup>-3</sup>). Further gas-phase aging is simulated  
121 through OH oxidation of SOA vapors with a fixed rate of  $1.0 \times 10^{-11}$  cm<sup>3</sup> molec<sup>-1</sup> s<sup>-1</sup>, with products shifted down one  
122 volatility bin (Murphy and Pandis, 2009), e.g., the condensable vapors with  $C^*$  of 1 μg m<sup>-3</sup> react with OH forming surrogate  
123 species in the lowest volatility bin ( $C^*$  of  $10^{-4}$  μg m<sup>-3</sup>). The partitioning of organic compounds between the gas and particle  
124 phases is simulated based on Pankow (1994) which is implemented in MOSAIC (Shrivastava et al., 2011). We apply glass



125 transition temperature and viscosity calculations to WRF-Chem model output for traditional SOA formed from the oxidation  
 126 of volatile organic compounds including alkanes, alkenes, aromatics, isoprene, and monoterpenes (Lane et al., 2008a).

## 127 2.2 Glass transition temperature and viscosity calculations

128 The glass-transition temperature of SOA products in each volatility bin at dry conditions ( $T_{g,i}$ ) is calculated as a function of  
 129 the saturation mass concentration at 298 K ( $C^0$ ) using the parameterization (Eq. 1) developed in our previous study (Li et al.,  
 130 2020). We assume ideal thermodynamic mixing that  $C^0$  is equal to  $C^*$ , which is often applied in the VBS (Donahue et al.,  
 131 2011).

$$132 \quad T_{g,i} = 288.70 - 15.33 \times \log_{10}(C^0) - 0.33 \times [\log_{10}(C^0)]^2 \quad (1)$$

133 The  $T_g$  of mixtures of dry SOA compounds ( $T_{g,org}$ ) is calculated by the Gordon–Taylor equation (Gordon and Taylor,  
 134 1952), with the Gordon–Taylor constant ( $k_{GT}$ ) assumed to be 1 (Dette et al., 2014):

$$135 \quad T_{g,org} = \sum_i \omega_i T_{g,i} \quad (2)$$

136 where  $\omega_i$  is the mass fraction of SOA products in each volatility bin simulated by the VBS module in WRF-Chem.

137 The particle phase state depends strongly on water content in particles, as water can act as a plasticizer to decrease  
 138 viscosity (Mikhailov et al., 2009; Koop et al., 2011). The mass concentration of water absorbed by SOA particles under  
 139 humid conditions is estimated using the effective hygroscopicity parameter ( $\kappa$ ) (Petters and Kreidenweis, 2007) as:

$$140 \quad m_{H_2O} = \left( \frac{a_w}{1 - a_w} \right) \frac{\kappa \rho_w m_{SOA}}{\rho_{SOA}} \quad (3)$$

141 where  $a_w$  is water activity calculated as  $a_w = RH/100$  and  $\rho_w$  is the density of water.  $m_{SOA}$  is the simulated total mass  
 142 concentrations of traditional SOA. The density of SOA particles ( $\rho_{SOA}$ ) is assumed to be  $1.5 \text{ g cm}^{-3}$  (Knote et al., 2015).  $\kappa$  is  
 143 assumed to be 0.1 based on previous studies (Gunthe et al., 2009; Duplissy et al., 2011; Wu et al., 2013) and consistent with  
 144 the value used in our previous global SOA phase state simulations (Shiraiwa et al., 2017).

145  $T_g$  of organic-water mixtures is also calculated by the Gordon–Taylor equation (Eq. 4) with  $k_{GT}$  suggested to be 2.5  
 146 (Koop et al., 2011).

$$147 \quad T_g(\omega_{org}) = \frac{(1 - \omega_{org})T_{g,w} + \frac{1}{k_{GT}}\omega_{org}T_{g,org}}{(1 - \omega_{org}) + \frac{1}{k_{GT}}\omega_{org}} \quad (4)$$

148 where  $\omega_{org}$  is the mass fraction of the simulated SOA species in organic-water mixtures. The glass transition temperature of  
 149 pure water ( $T_{g,w}$ ) is 136 K (Kohl et al., 2005). Based on  $T_g(\omega_{org})$ , viscosity can be calculated with the  
 150 Vogel–Tammann–Fulcher (VTF) equation (Angell, 1991):  $\eta = \eta_\infty e^{\frac{T_0 D}{T - T_0}}$ , where  $\eta_\infty$  is the viscosity at infinite temperature  
 151 ( $10^{-5} \text{ Pa s}$ , Angell (1991)).  $D$  is the fragility parameter which is adopted to be 10 based on our previous study in DeRieux and



152 Li et al. (2018).  $T_0$  is the Vogel temperature calculated as  $T_0 = \frac{39.17T_g(\omega_{org})}{D+39.17}$ . We further calculate the bulk diffusion  
153 coefficient ( $D_b$ ) of organic molecules with a radius of 0.4 nm (Maclean et al., 2021) and water molecules in SOA particles  
154 based on predicted viscosity and the fractional Stokes–Einstein equation (Price et al., 2016; Evoy et al., 2019; Evoy et al.,  
155 2020), which is detailed in the Supplement. The mixing timescales of molecules ( $\tau_{mix}$ ) within SOA particles is calculated as  
156  $\tau_{mix} = d_p^2/(4\pi^2D_b)$  (Seinfeld and Pandis, 2016), where  $d_p$  is the particle diameter. The  $d_p$  is assumed to be 200 nm  
157 (Maclean et al., 2021) when we calculate  $\tau_{mix}$ .

### 158 2.3 Sensitivity simulations

159 Table 1 lists all the performed simulations. In the base case, we update the  $C^*$  in the lowest volatility bin from  $10^{-4} \mu\text{g m}^{-3}$  in  
160 the official WRF-Chem v3.7.1 to  $0.1 \mu\text{g m}^{-3}$  based on the ambient volatility observations (referring to Section 2.4 and Fig. 1),  
161 and calculate the  $\Delta H_{vap}$  in the lowest volatility bin using the semi-empirical parameterization in Epstein et al. (2010), leading  
162 to a value of  $142 \text{ kJ mol}^{-1}$ . To evaluate the effects of simulated SOA volatility distributions on phase state estimations, we  
163 conduct a simulation (sensitivity case A) following the default setting in the model assuming that the lowest  $C^*$  is  $10^{-4} \mu\text{g m}^{-3}$   
164 at 298 K, with  $\Delta H_{vap}$  of  $40 \text{ kJ mol}^{-1}$  (Knote et al., 2015). A smaller  $\Delta H_{vap}$  indicates less dependence of volatility on  
165 temperature variations. In the sensitivity case B, we increase the simulated RH by a factor of 10 % as we find that the  
166 simulated RH values are smaller than the observations (Section 3.1). In the base case and sensitivity cases A and B, we  
167 predict  $T_g$  for SOA-water mixtures accounting for the SOA-influenced water uptake solely, assuming that SOA particles are  
168 externally mixed with inorganic compounds such as sulfate and nitrate. In the sensitivity case C, we assume that the organic  
169 and inorganic compounds are always internally mixed in one phase and include the water absorbed by inorganic compounds  
170 in viscosity calculations. The water associated with inorganics is calculated by the MOSAIC module coupled in WRF-Chem.

### 171 2.4 Observation

172 The observation data measured at an urban site in the Institute of Atmospheric Physics (IAP), Chinese Academy of Sciences  
173 ( $39^\circ 58' 28'' \text{ N}$ ,  $116^\circ 22' 16'' \text{ E}$ ) in Beijing (Fig. S1) are used to compare with the simulation results of the WRF-Chem model.  
174 The aerosol volatility was measured from 20 May to 23 June in 2018, using a thermodenuder coupled with an Aerodyne  
175 high-resolution aerosol mass spectrometer (Xu et al., 2019). The volatility distributions of oxygenated organic aerosols  
176 (OOA) resolved from positive matrix factorization (PMF) were estimated using a dynamic mass transfer model (Riipinen et  
177 al., 2010). The volatility of OOA was found to be distributed in six logarithmically spaced  $C^*$  bins including 0.001, 0.01, 0.1,  
178 1, 10, and  $100 \mu\text{g m}^{-3}$ , based on the best fits between the measured and predicted thermograms using the methods in Karnezi  
179 et al. (2014). Chemical species including organics (Org), sulfate ( $\text{SO}_4^{2-}$ ), nitrate ( $\text{NO}_3^-$ ), and ammonium ( $\text{NH}_4^+$ ) in  $\text{PM}_{2.5}$   
180 were measured using an Aerodyne time-of-flight aerosol chemical speciation monitor (Fröhlich et al., 2013) equipped with a  
181 capture vaporizer and  $\text{PM}_{2.5}$  lens, with the details described in Li et al. (2023). The OOA factor was identified with the PMF



182 analysis. We obtain the mass concentrations of PM<sub>2.5</sub> from the Olympic Center observation site (<http://zx.bjmemc.com.cn>)  
183 which is ~4 km from the IAP site (Fig. S1). Meteorological parameters including RH and *T* are from the Beijing  
184 meteorological tower at the IAP site.

### 185 3 Results

#### 186 3.1 Simulations in Beijing and the comparison with observations

187 The comprehensive model evaluations were conducted in our previous studies, showing that the WRF-Chem model  
188 reasonably captured the magnitudes and spatial distributions of concentrations of major air pollutants over China (Li et al.,  
189 2011; Li et al., 2014; Li et al., 2015; Qu et al., 2019; Zhang et al., 2022). Here we focus on the comparison of simulations  
190 and observations at the IAP site during 20 May – 23 June 2018 when the observed volatility distributions are available (Xu et  
191 al., 2019).

192 Figure 1 shows the average volatility distributions of observed OOA and simulated SOA at the IAP site. The *C\** of OOA  
193 spans from 0.001 μg m<sup>-3</sup> to 100 μg m<sup>-3</sup>, with an average value of 1.16 μg m<sup>-3</sup>. The semi-volatile organic compounds (SVOC;  
194 0.3 < *C*<sup>0</sup> < 300 μg m<sup>-3</sup>) and the low-volatile organic compounds (LVOC; 3×10<sup>-4</sup> < *C*<sup>0</sup> < 0.3 μg m<sup>-3</sup>) (Donahue et al., 2012)  
195 contribute 66.3 % and 33.7 % to OOA concentrations, respectively (Xu et al., 2019). The *T*<sub>g,org</sub> estimated from the observed  
196 OOA volatility distributions is 286.7 K. Figure 1a shows the simulated volatility distributions of SOA with five *C\** bins set to  
197 be 0.1, 1, 10, 100, and 1000 μg m<sup>-3</sup> at 298 K, and Δ*H*<sub>vap</sub> of 142, 131, 120, 109, and 98 kJ mol<sup>-1</sup> used in the five *C\** bins,  
198 respectively (base case in Table 1). In this base case simulation, the SOA consists of 64.5 % SVOC and 35.3 % LVOC, and  
199 most of the SVOC species are located in the *C\** bin of 1 μg m<sup>-3</sup>. The simulated SOA in Fig. 1a has an average *C\** of 0.64 μg  
200 m<sup>-3</sup> and *T*<sub>g,org</sub> of 291.5 K, close to the values estimated from the volatility distributions of OOA. Figure 1b shows the  
201 simulated volatility distributions of SOA with the lowest *C\** bin set to be 0.0001 μg m<sup>-3</sup> at 298 K with Δ*H*<sub>vap</sub> of 40 kJ mol<sup>-1</sup>,  
202 following the default option in the official WRF-Chem model 3.7.1 (Knote et al., 2015). In this sensitivity simulation (case A  
203 in Table 1), the SOA consists of 40.4 % extremely low-volatile organic compounds (ELVOC; *C*<sup>0</sup> < 3×10<sup>-4</sup> μg m<sup>-3</sup>), which are  
204 not determined in the observed OOA, leading to a much lower average *C\** (0.03 μg m<sup>-3</sup>) and a higher *T*<sub>g,org</sub> (309.0 K)  
205 compared to the observations. In the following we estimate the *T*<sub>g,org</sub> and viscosity of SOA using the simulated volatility  
206 distributions in the base case with the lowest *C\** bin set as 0.1 μg m<sup>-3</sup> at 298 K. The impacts of volatility distributions with  
207 the incorporation of ELVOC (Fig. 1b) on viscosity estimations are evaluated in section 3.3.

208 Figure 2 shows that the model relatively well reproduces the observed hourly variations of RH, *T*, mass concentrations  
209 of PM<sub>2.5</sub> and its major inorganic components (Figs. 2a – f), with the index of agreement (IOA, defined in the supplement)  
210 varied from ~0.70 for inorganic components to a higher value of 0.93 for *T* (Table S2). The simulated values of RH are  
211 constantly lower than the observations, with the mean bias (MB) being -10.97 % (Table S2). The underestimation of RH



212 observations was also found at other meteorological sites in the North China Plain in our previous studies (Qu et al., 2019;  
213 Zhang et al., 2022), which would affect the SOA viscosity estimations. The effects of RH on the viscosity estimations are  
214 evaluated in section 3.3. Figure 2g shows that the model could generally reproduce the observed temporal variations of OOA  
215 concentrations, but largely underestimates the observation peaks ( $MB = -5.88 \mu\text{g m}^{-3}$ , the normalized mean bias  $NMB = -$   
216  $53.28 \%$ , Table S2). Incorporation of the SOA formed from intermediate-volatile organic compounds (IVOCs) (Miao et al.,  
217 2021; Chang et al., 2022) would increase the simulated SOA concentrations, which is beyond the scope of this study and will  
218 be considered in our future work. The simulated SOA mean concentration is  $5.15 \mu\text{g m}^{-3}$ . Although it is lower than the  
219 observed value of  $11.03 \mu\text{g m}^{-3}$ , this difference in the simulated and observed SOA concentrations would not affect the  
220 viscosity predictions significantly. The SOA viscosity has a much closer relation with the volatility rather than its mass  
221 loadings (Li et al., 2020; Champion et al., 2019). In our previous study we estimated  $T_{g,org}$  and viscosities at different OA  
222 mass loadings varied from 1 to  $1000 \mu\text{g m}^{-3}$ , showing that the simulated viscosities were very similar, particularly when RH  
223 was higher than 50 % (Derieux et al., 2018).

224 As the WRF-Chem model underestimates the observed RH at the IAP site, we calculate the SOA viscosity using the  
225 simulated and observed RH, respectively. Figure 2h shows that the viscosities calculated at the two conditions are similar at  
226 most times during the simulated period, ranging mainly from  $\sim 10^2 \text{ Pa s}$  to  $10^{10} \text{ Pa s}$ , with a median value of  $\sim 10^7 \text{ Pa s}$ ,  
227 indicating that a semi-solid phase state frequently occurs. The underestimations of the observed RH by WRF-Chem mainly  
228 impact the phase state estimations at relatively high RH. For example, SOA particles occur as liquid when the observed RH  
229 is higher than  $\sim 75 \%$ ; however, they remain in a semi-solid phase state at the simulated RH. The bulk diffusion coefficients  
230 ( $D_b$ ) of organic molecules range from  $10^{-18}$  to  $10^{-11} \text{ cm}^2 \text{ s}^{-1}$  at the simulated RH (Fig. 2i), leading to the mixing timescales  
231 within 200 nm SOA particles being seconds to years, with 61 % of the time  $> 1$  hour (Fig. S2).

232 The vertical profiles of SOA viscosity exhibit diurnal variations. Figure 3a shows the median diurnal and vertical  
233 profiles of predicted SOA viscosity at the IAP site. The SOA particles remain highly viscous ( $\sim 10^7 - 10^8 \text{ Pa s}$ ) at the surface,  
234 with a higher viscosity occurring from late afternoon to early evening, during which the RH is less than 20 %, lower than the  
235 rest time of the day (Fig. S3). The SOA particles become more viscous at higher altitudes than the surface and adopt the  
236 phase transition from a semi-solid phase to a solid phase at  $\sim 4 \text{ km}$  at the IAP site. The predicted altitude with the phase  
237 transition is  $\sim 2 \text{ km}$  higher than our previous global model prediction for the region of East China which was an average of  
238 five years' simulations (Shiraiwa et al., 2017). Tan et al. (2020) inferred the phase state of submicrometer particles in Beijing  
239 from the surface to an altitude of  $\sim 1 \text{ km}$  using a polarization lidar and found that the particle phase state exhibits a vertical  
240 variation. Further observations of SOA viscosity at high altitudes are needed to better understand the viscosity vertical  
241 profiles and validate our predictions. Figure 3b shows that the mixing timescales for organic molecules within 200 nm SOA  
242 particles are approximately 1 hour at the surface, and longer than  $\sim 10$  hours at altitudes higher than 1 km, indicating that  
243 kinetic limitations in the gas-particle partitioning may be required to accurately predict SOA mass concentrations in summer





244 Beijing, particularly in the upper planetary boundary layer and the free troposphere.

### 245 **3.2 Simulated glass transition temperature and viscosity of SOA particles over China**

246 The glass transition temperature of the dry organic phase ( $T_{g,org}$ ) shows a geospatial gradient over China. Figure 4a shows the  
247 median surface values of  $T_{g,org}$  calculated in the base simulation (Table 1).  $T_{g,org}$  ranges from  $\sim 287 - 305$  K over most areas of  
248 China, with lower values occurring mainly over the southeast and higher values over the northwest. The  $T_{g,org}$  range  
249 simulated by the WRF-Chem model is consistent with our previous global simulations of  $T_{g,org}$  that varied from  $\sim 285$  K to  
250  $310$  K at the surface over China (Shiraiwa et al., 2017). The geospatial variation in  $T_{g,org}$  is related to the simulated SOA  
251 volatility distributions. Figure 4b shows the mass fractions of SOA species distributed in the lowest volatility bin (SOAX  
252 with  $C^* = 0.1 \mu\text{g m}^{-3}$  at  $298$  K). The mass fractions of SOAX are mostly  $20 - 35\%$  in the southeastern China, indicating that  
253 the majority of the simulated SOA formed from VOCs is semi-volatile. In these areas, the simulated SOA mass  
254 concentrations are higher than the other locations of China (Fig. S4) (Li et al., 2022), which is favorable for more SVOCs  
255 partitioning into the particle phase, leading to relatively low values of  $T_{g,org}$  (Fig. 4a). LVOCs are more frequently contained  
256 in aged SOA particles in remote areas, e.g., some areas in the northwestern China where the SOA mass concentrations are  
257 very low, resulted in higher  $T_{g,org}$  values.

258 The relative humidity plays an important role in regulating SOA viscosity (Koop et al., 2011). Considering the water  
259 uptake by SOA particles in the phase state estimations, the predicted geospatial patterns in the viscosity (Fig. 5a) and RH  
260 (Fig. S4) are very similar with each other, particularly in southern and northeastern China. SOA particles are predicted to  
261 mainly be liquid or with a low viscosity ( $< 10^4$  Pa s) in the southeast. Figure 5b shows the frequency of liquid phase state,  
262 which is calculated as the percent time that an organic aerosol particle is in the liquid phase state during the simulated period.  
263 The frequency of liquid particles varies from  $\sim 30\%$  to  $70\%$  in the southeastern China. The lowest viscosity with the highest  
264 frequency of liquid particles occurs over the southern Tibetan Plateau where RH is very high (Fig. S4), which is contributed  
265 by summer monsoons and regional moisture recycling (Dong et al., 2016). The SOA particles in the central and northeastern  
266 China are predicted to be semi-solid, with the viscosity varied from  $10^5$  to  $10^8$  Pa s (Fig. 5a). Highly viscous ( $\eta > 10^8$  Pa s) or  
267 solid SOA particles are mainly found in the northwest, particularly over the northern Tibetan Plateau where the ambient  
268 temperatures are lower than other areas of China (Fig. S4). The frequency of liquid SOA particles in most areas with the  
269 latitude higher than  $30^\circ\text{N}$  is less than  $20\%$  (Fig. 5b).

270 The simulated geospatial pattern in SOA viscosity over China agrees with previous global simulations and ambient  
271 measurements. Our previous global simulations predicted a lower viscosity ( $\eta < 10^3$  Pa s) in SOA particles in southeastern  
272 China and a higher viscosity ( $\eta > 10^8$  Pa s) in northwestern China (Shiraiwa et al., 2017; Li et al., 2020), similar to the  
273 WRF-Chem simulations in this study. Interestingly, the occurrence of liquid particles over the southern Tibetan Plateau in  
274 summer simulated by the WRF-Chem was not found in our previous global predictions, which was an average of five years'



275 simulations. The semi-solid phase state of SOA particles simulated in Beijing is consistent with both particle bounce  
276 measurements (Liu et al., 2017) and the  $PM_{2.5}$  phase state determined by the poke-and-flow technique (Song et al., 2022).  
277 The simulated viscosity of SOA particles is 0.15 Pa s in Shenzhen, a coastal urban city in southeastern China, which also  
278 agrees with the findings in the previous bounce measurements indicating that the submicron particles in Shenzhen are in the  
279 liquid state (Liu et al., 2019).

280 Figure 5c shows the median values of viscosity as a function of RH calculated for selected regions in the northern China,  
281 southern China, northern Qinghai-Tibet Plateau, and southern Qinghai-Tibet Plateau as specified by white boxes in Fig. 5a.  
282 There is a strong inverse relationship between SOA viscosity and relative humidity with high RH ( $> \sim 60\%$ ) as the dominant  
283 factor determining the phase state of SOA particles. When RH is lower than  $\sim 60\%$ , the predicted viscosity is affected by  
284 both RH and  $T$ . For example, the SOA particles occur mainly as solid over the Northern Qinghai-Tibet Plateau while occur  
285 as semi-solid over the Northern China within similar RH ranges ( $20\% < RH < 60\%$ ); the reason is that the ambient  $T$  over  
286 the Northern Qinghai-Tibet Plateau is much lower ( $\sim 20$  K lower) than the Northern China (Fig. S5a). When RH is relatively  
287 low, the viscosity of SOA particles is also influenced by particle chemical composition, i.e., the SOA particles composed of  
288 high mass fractions of low volatility compounds tend to have higher viscosity values (Fig. S5b). RH is the main factor  
289 driving the diurnal variations of SOA viscosity in our simulations. Figure S6 shows that SOA particles have higher viscosity  
290 in the daytime than the nighttime as RH in the daytime is lower than the nighttime (Fig. S7). Compared to the northern China,  
291 the southern China exhibits stronger diurnal variations in SOA viscosity that SOA particles occur mainly as semi-solid in the  
292 daytime and liquid in the nighttime. Highly viscous or solid SOA particles are found in the northern China during both  
293 daytime and nighttime (Fig. S6).

294 The bulk diffusion coefficient is an important parameter determining the mass-transport and mixing rates, which can be  
295 predicted by the particle viscosity through the fractional Stokes-Einstein relation (see the Method). The  $D_b$  of organic  
296 molecules is predicted to be  $> \sim 10^{-10} \text{ cm}^2 \text{ s}^{-1}$  in the southern China. The highest value is  $\sim 10^{-5} \text{ cm}^2 \text{ s}^{-1}$  occurring in liquid  
297 SOA particles in the southern Tibetan Plateau (Fig. 6a). The  $D_b$  of organic molecules within semisolid SOA particles is  $\sim 10^{-18}$   
298  $- 10^{-10} \text{ cm}^2 \text{ s}^{-1}$  in the central and northeastern China, and lower than  $\sim 10^{-18} \text{ cm}^2 \text{ s}^{-1}$  in highly viscous and solid particles in  
299 most areas of the northwestern China. Figure 6b shows the percent time that the mixing timescale of organic molecules in  
300 200 nm particles is less than 1 h in the entire simulation period. The mixing timescale is found nearly always less than 1 h in  
301 the southeastern region of the “Hu Huanyong Line”. The “Hu Huanyong Line”, proposed by the Chinese geographer  
302 Huanyong Hu, divides China into two parts based on contrasting population densities (Hu, 1935), which was found also  
303 useful characterizing the drought conditions, with the northwestern region much dryer than the southeastern region (Zeng et  
304 al., 2021). The mixing timescale of organic molecules in highly viscous or solid SOA particles in the northwest of the “Hu  
305 Huanyong Line” is often longer than 1 h (the frequency  $> 70\%$ ), indicating that in these areas kinetic limitations of bulk  
306 diffusion should be considered in SOA partitioning. Compared to the diffusion coefficients of organic molecules, the  $D_b$  of



307 water molecules in SOA particles at the surface is several orders of magnitude larger, with the values higher than  $10^{-10} \text{ cm}^2 \text{ s}^{-1}$   
308  $^{-1}$  in the southeast, and as low as  $\sim 10^{-13} \text{ cm}^2 \text{ s}^{-1}$  in the northwestern China (Fig. 6c). The mixing timescales of water  
309 molecules in SOA particles with a diameter of 200 nm are of the order of milliseconds in the southeast and seconds in the  
310 northwest of China (Fig. S8), indicating that the activation of cloud condensation nuclei would not be inhibited, in agreement  
311 with our previous global simulations (Shiraiwa et al., 2017).

312 Figure 7 shows the simulated  $T_{\text{g,org}}$  and the phase state of SOA particles, as well as the mixing timescale of organic  
313 molecules in SOA particles at 500 hPa. The  $T_{\text{g,org}}$  ranges from  $\sim 285 \text{ K} - 295 \text{ K}$ , lower than the  $T_{\text{g,org}}$  simulated at the surface  
314 (Fig. 7a). The reason is that the mass fractions of LVOCs (SOAX with  $C^*$  of  $0.1 \mu\text{g m}^{-3}$  at 298 K) at 500 hPa (Fig. S9) are  
315 smaller than the surface values (Fig. 4b). The low temperature at 500 hPa is favorable for SVOCs partitioned into the particle  
316 phase, thus compared to the surface conditions, there is less semi-volatile vapors undergoing the further gas-phase aging  
317 forming SOAX species. The percent time that an organic aerosol particle is in the liquid phase state (the frequency of liquid  
318 SOA particles) at 500 hPa in the southeastern China is 20 – 35 % (Fig. 7b), which is  $\sim 20 \%$  lower than the surface values  
319 (Fig. 5b). In the northern China, the frequency of liquid SOA particles at 500 hPa is similar to the results at the surface,  
320 which is related to the RH spatial patterns (Fig. S10). The mixing timescale of organic molecules in 200 nm SOA particles is  
321 frequently longer than 1 h at 500 hPa, with the frequency  $> 70 \%$  in the northern China and  $\sim 40 \%$  in the southeastern China  
322 (Fig. 7c). The  $\tau_{\text{mix}}$  is relatively short (the frequency of  $\tau_{\text{mix}} \leq 1 \text{ h}$  being  $\sim 80 \%$ ) in some areas of the southwestern China at  
323 500 hPa, where relatively high RH could occur (Fig. S10) in the season of summer monsoon (Huang et al., 1998).

### 324 3.3 Sensitivity simulations

#### 325 3.3.1 Impacts of volatility distributions on phase state estimations

326 The volatility and viscosity of organic aerosols are closely related (Rothfuss and Petters, 2017; Shiraiwa et al., 2017;  
327 Champion et al., 2019; Zhang et al., 2019b; Li et al., 2020). In this section we conduct sensitivity simulations (case A, Table  
328 1) to evaluate how the simulated volatility distributions affect the phase state estimations. The lowest  $C^*$  bin in the base case  
329 is  $0.1 \mu\text{g m}^{-3}$  at 298 K, with  $\Delta H_{\text{vap}}$  of  $142 \text{ kJ mol}^{-1}$ , which does not incorporate ELVOC species at the room temperature. The  
330 sensitivity simulation (case A) adopts the default setting in the official WRF-Chem model v3.7.1, assuming that the lowest  
331  $C^*$  is  $0.0001 \mu\text{g m}^{-3}$  at 298 K, with  $\Delta H_{\text{vap}}$  of  $40 \text{ kJ mol}^{-1}$  (Knote et al., 2015). Figure 8 shows that including these ELVOCs at  
332 298 K with a relatively small  $\Delta H_{\text{vap}}$  mainly affect the  $T_{\text{g,org}}$  simulated over remote areas, e.g., the northwestern China and the  
333 marine areas, where the simulated  $T_{\text{g,org}}$  is increased by 30 – 40 K (Fig. 8a). In other regions of China, the changes in  $T_{\text{g,org}}$   
334 are less than 25 K. Although consideration of these ELVOCs could affect the simulated  $T_{\text{g,org}}$  at the surface obviously in  
335 remote areas, i.e., the northwestern China, it does not impact the predicted frequency of the occurrence of a liquid phase state  
336 (Fig. 8b), as in these dry areas the SOA particles are highly viscous. Including ELVOC formation at 298 K ( $\Delta H_{\text{vap}}$  of  $40 \text{ kJ}$   
337  $\text{mol}^{-1}$ ) mainly affects the phase state estimations in areas with a moderate humidity. For example, in some areas of the



338 southeastern China with ~ 70 % RH, the SOA particles are predicted to be more viscous, with the frequency of a liquid phase  
339 state decreasing by up to 12 % (Fig. 8b). These results indicate that the SOA phase state estimations in the base and  
340 sensitivity case A are generally in agreement in the simulated episode in this study. Ambient measurements of organic  
341 aerosol volatility distributions are still sparse over China. A recent field study showed that the ELVOCs contributed more  
342 than half to the OA mass observed at a regional background site near the Bohai Sea (Feng et al., 2023), which resulted in an  
343 estimated viscosity much higher than our WRF-Chem simulations. More field volatility distribution measurements should be  
344 conducted over China to further evaluate the effects of ELVOCs and how to choose reasonable values of the enthalpy of  
345 vaporization that would affect phase state estimations.

### 346 **3.3.2 Impacts of RH and the water absorbed by inorganics on phase state estimations**

347 RH is an important parameter affecting the phase state estimations. We perform a sensitivity calculation (case B, Table 1)  
348 with the simulated RH increased by a factor of 10 % to compensate for the fact that the current model underestimates the  
349 observed RH as shown in Fig. 2 and found in our previous simulations (Qu et al., 2019; Zhang et al., 2022). The increases in  
350 simulated RH lead to more occurrence (the liquid frequency increased by 10 – 20 %) of liquid SOA particles in southeastern  
351 China where the predicted RH is ranged mainly from 70 to 80 % (Fig. S4), with very limited effects in phase state  
352 predictions in relatively dry areas, e.g., the northern China (Fig. 9a). Besides RH, the water absorbed by inorganic species  
353 present in atmospheric particles also plays an important role in the phase state of ambient particles (Marcolli and Krieger,  
354 2006). Here we perform a sensitivity calculation (case C, Table 1) assuming that the organic and inorganic compounds are  
355 always internally mixed in one phase, which can be regarded that the predicted viscosity is at the lower end of the viscosity  
356 in real ambient particles. Figure 9b shows that including the water absorbed by inorganic species can significantly lower the  
357 simulated viscosity over most areas of China, with the liquid frequency increased by 15 – 45 % in the southeast, and 5 – 15 %  
358 in some areas of the northeast. The effects over dry lands in the northwestern China are relatively small.

## 359 **4 Conclusions and discussions**

360 We simulate the glass transition temperature and viscosity of SOA particles over China based on SOA volatility using the  
361 WRF-Chem model. This is the first time that spatial variations in the SOA phase state over China are investigated by a  
362 regional chemical transport model. Simulations show that  $T_g$  values of dry SOA ( $T_{g,org}$ ) range from ~287 K to 305 K over  
363 most areas of China at the surface, which is consistent with our previous simulated results based on a global transport model  
364 (Shiraiwa et al., 2017). The  $T_{g,org}$  is higher in the northwestern China than the southeastern China. This geospatial variation in  
365  $T_{g,org}$  is related to the simulated SOA volatility distributions that SOA particles in northwestern China have relatively low  
366 volatilities. Considering the water uptake by SOA particles, the SOA viscosity also shows a prominent geospatial gradient  
367 that highly viscous or solid SOA particles are mainly found in the northwestern China. The frequency of liquid SOA particles



368 in most areas with the latitude higher than 30°N is less than 20 %. The lowest and highest SOA viscosities both occur over  
369 the Qinghai-Tibet Plateau, with the solid phase state predicted over dry and high-altitude areas and the liquid phase state  
370 predicted mainly in the south of the plateau with high RH in the summer. This indicates that this area has very large spatial  
371 variation in SOA phase state, which was not found in our previous global simulations. We recommend measurements in  
372 ambient particle phase state to be conducted over the Qinghai-Tibet Plateau, one of the most sensitive regions to climate  
373 change (Liu and Chen, 2000).

374 The mixing timescale of organic molecules in 200 nm SOA particles is calculated based on the simulated particle  
375 viscosity and the bulk diffusion coefficients of organic molecules. Calculations show that at the surface and at 500 hPa, the  
376 percent time of  $\tau_{\text{mix}}$  longer than 1 h is  $> \sim 70$  % in the northwest of the “Hu Huanyong Line”. When the mixing timescales of  
377 organics are greater than roughly 1 h, which is longer than the typical time step in CTMs, the instantaneous equilibrium  
378 partitioning usually assumed in SOA formation simulations is subject to be re-evaluated. The kinetic partitioning considering  
379 the bulk diffusion in viscous particles may be required for more accurate prediction of SOA mass concentrations and size  
380 distributions over the areas with long mixing timescale of organic molecules (Shiraiwa and Seinfeld, 2012; Zaveri et al.,  
381 2018; Li and Shiraiwa, 2019; Zaveri et al., 2020; He et al., 2021; Maclean et al., 2021; Jathar et al., 2021; Shrivastava et al.,  
382 2022).

383 The  $T_{\text{g,org}}$  calculations in the base simulation are based on simulated volatility distributions of SOA formed from VOCs,  
384 with five  $C^*$  bins of 0.1, 1, 10, 100, and 1000  $\mu\text{g m}^{-3}$  at 298 K, with  $\Delta H_{\text{vap}}$  of 142, 131, 120, 109, and 98  $\text{kJ mol}^{-1}$  used in the  
385 five  $C^*$  bins, respectively. The average  $C^*$  and  $T_{\text{g,org}}$  of the simulated SOA agree well with the values estimated from ambient  
386 measurements of OOA volatilities at the IAP site in Beijing, where ELVOCs were not determined in the observed OOA (Xu  
387 et al., 2019). We run a sensitivity simulation considering ELVOCs, with the lowest volatility bin having the  $C^*$  of 0.0001  $\mu\text{g}$   
388  $\text{m}^{-3}$  at 298 K and the  $\Delta H_{\text{vap}}$  of 40  $\text{kJ mol}^{-1}$ , following Knote et al. (2015). The sensitivity simulation shows that compared to  
389 the base simulation, the frequency of a liquid phase state does not change in most areas of China, and incorporation of  
390 ELVOCs mainly have a limited effect making SOA particles more viscous in some areas of the southeastern China. Our  
391 previous study ever found that the  $T_{\text{g,org}}$  of total OA in the SOAS (Southern Oxidant and Aerosol Study) campaign could  
392 have a large variation (from 232 to 334 K) (Li et al., 2020) as the volatility distributions derived from different methods  
393 could be different (Stark et al., 2017). The most credible predicted  $T_{\text{g,org}}$  values were screened to be 313 – 330 K during the  
394 SOAS campaign based on the most atmospherically relevant volatility distributions (Li et al., 2020). The volatility  
395 distributions of organic aerosols derived from ambient volatility measurements are still limited over China (Xu et al., 2021;  
396 Liu et al., 2021a; Feng et al., 2023). It needs more field volatility measurements to evaluate the effects of ELVOCs as well as  
397 the enthalpy of vaporization on OA phase state estimations over China.

398 In the base simulation we assume that SOA components are phase separated from inorganic compounds in fine particles,  
399 in which way the organic-rich and inorganic-rich phases may undergo phase transition separately (Dette and Koop, 2015).



400 This is consistent to recent ambient observations showing that the phase separation with an organic-rich shell and an  
401 inorganic core was a frequent phenomenon in individual particles (diameters > 100 nm) collected over the North China Plain  
402 (Li et al., 2021a). Previous simulations conducted for the SOAS campaign also showed that the phase separation was  
403 expected ~ 65 % of the time on average (Schmedding et al., 2020), and exhibited a diurnal variation with a relation with the  
404 predicted O:C ratio and RH (Pye et al., 2017). From a sensitivity simulation assuming that the organic and inorganic  
405 compounds are always internally mixed in one phase, we show that the water absorbed by inorganic species has a significant  
406 impact lowering the simulated viscosity over the southeastern China. At such mixing condition with one phase, on one hand,  
407 it is expected that the inorganic salts that often have lower  $T_g$  compared to SOA compounds would further lower the particle  
408 viscosity relative to the organic fraction alone (Dette and Koop, 2015). On the other hand, the presence of divalent inorganic  
409 ions could increase the viscosity of mixed organic-inorganic particles, enabling a humidity-dependent gel phase transition  
410 through cooperative ion-molecule interactions (Richards et al., 2020). For complex mixtures of primary OA, SOA and  
411 inorganics, it was found that three distinct phases could occur (Huang et al., 2021). Solid organic-coated ammonium sulfate  
412 particles were observed at high RH in the summertime Arctic atmosphere, which may be formed from contact efflorescence  
413 during collision of an Aitken mode sulfate particle with an organic-coated ammonium sulfate particle (Kirpes et al., 2022).  
414 Kinetic simulations of the condensation of SVOCs into a core-shell phase-separated particle showed that the interplay of  
415 non-ideality and phase state can impact SOA partitioning kinetics significantly (Schervish and Shiraiwa, 2023). The impacts  
416 of the complex interplay of organic and inorganic compounds on the phase state of multicomponent particles in ambient air  
417 warrant further investigations in future studies (Lilek and Zuend, 2022).

418 *Data availability.* The simulation data in this study are available upon request from the corresponding author  
419 ([living-iap@mail.iap.ac.cn](mailto:living-iap@mail.iap.ac.cn)).

420 *Supplement.* The supplement related to this article is available on-line.

421 *Author contributions.* YL and MS designed the research. ZZ, HR, and YQ performed the WRF-Chem modeling. ZZ, YL,  
422 and HR analyzed the simulation data. WZ, WX, WH, and YS provided observation data. YL, ZZ, and MS wrote the  
423 manuscript. ZZ, YL, and HR wrote the supplement. All authors discussed the results and contributed to the article editing.

424 *Competing interests.* At least one of the (co-)authors is a member of the editorial board of Atmospheric Chemistry and  
425 Physics. The peer-review process was guided by an independent editor, and the authors have also no other competing  
426 interests to declare.

427 *Acknowledgements.* This work was supported by the National Natural Science Foundation of China (grant no. 42075110).  
428 The authors thank Qi Chen at the Peking University and Bin Zhao at the Tsinghua University for insightful suggestions on



429 SOA volatility simulations in this work.

430 *Financial support.* This work was supported by the National Natural Science Foundation of China (grant no. 42075110).

#### 431 **References**

- 432 Abbatt, J. P. D., Lee, A. K. Y., and Thornton, J. A.: Quantifying trace gas uptake to tropospheric aerosol: recent advances and  
433 remaining challenges, *Chem. Soc. Rev.*, 41, 6555-6581, <https://doi.org/10.1039/C2CS35052A>, 2012.
- 434 Ahmadov, R., McKeen, S. A., Robinson, A. L., Bahreini, R., Middlebrook, A. M., de Gouw, J. A., Meagher, J., Hsie, E. Y.,  
435 Edgerton, E., Shaw, S., and Trainer, M.: A volatility basis set model for summertime secondary organic aerosols over  
436 the eastern United States in 2006, *J. Geophys. Res.: Atmos.*, 117, <https://doi.org/10.1029/2011JD016831>, 2012.
- 437 Angell, C. A.: Relaxation in liquids, polymers and plastic crystals — strong/fragile patterns and problems, *J. Non-Cryst.*  
438 *Solids*, 131-133, 13-31, [https://doi.org/10.1016/0022-3093\(91\)90266-9](https://doi.org/10.1016/0022-3093(91)90266-9), 1991.
- 439 Baboomian, V. J., Crescenzo, G. V., Huang, Y., Mahrt, F., Shiraiwa, M., Bertram, A. K., and Nizkorodov, S. A.: Sunlight can  
440 convert atmospheric aerosols into a glassy solid state and modify their environmental impacts, *P. Natl. Acad. Sci. USA*,  
441 119, e2208121119, <https://doi.org/10.1073/pnas.2208121119>, 2022.
- 442 Champion, W. M., Rothfuss, N. E., Petters, M. D., and Grieshop, A. P.: Volatility and viscosity are correlated in terpene  
443 secondary organic aerosol formed in a flow reactor, *Environ. Sci. Technol. Lett.*, 6, 513-519,  
444 <https://doi.org/10.1021/acs.estlett.9b00412>, 2019.
- 445 Chang, X., Zhao, B., Zheng, H., Wang, S., Cai, S., Guo, F., Gui, P., Huang, G., Wu, D., Han, L., Xing, J., Man, H., Hu, R.,  
446 Liang, C., Xu, Q., Qiu, X., Ding, D., Liu, K., Han, R., Robinson, A. L., and Donahue, N. M.: Full-volatility emission  
447 framework corrects missing and underestimated secondary organic aerosol sources, *One Earth*, 5, 403-412,  
448 <https://doi.org/10.1016/j.oneear.2022.03.015>, 2022.
- 449 Dalton, A. B. and Nizkorodov, S. A.: Photochemical degradation of 4-nitrocatechol and 2,4-dinitrophenol in a sugar-glass  
450 secondary organic aerosol surrogate, *Environ. Sci. Technol.*, 55, 14586-14594, <https://doi.org/10.1021/acs.est.1c04975>,  
451 2021.
- 452 DeRieux, W. S. W., Li, Y., Lin, P., Laskin, J., Laskin, A., Bertram, A. K., Nizkorodov, S. A., and Shiraiwa, M.: Predicting the  
453 glass transition temperature and viscosity of secondary organic material using molecular composition, *Atmos. Chem.*  
454 *Phys.*, 18, 6331-6351, <https://doi.org/10.5194/acp-18-6331-2018>, 2018.
- 455 Dette, H. P. and Koop, T.: Glass formation processes in mixed inorganic/organic aerosol particles, *J. Phys. Chem. A*, 119,  
456 4552-4561, <https://doi.org/10.1021/jp5106967>, 2015.
- 457 Dette, H. P., Qi, M., Schröder, D. C., Godt, A., and Koop, T.: Glass-forming properties of 3-methylbutane-1,2,3-tricarboxylic  
458 acid and its mixtures with water and pinonic acid, *J. Phys. Chem. A*, 118, 7024-7033,  
459 <https://doi.org/10.1021/jp505910w>, 2014.
- 460 Donahue, N., Robinson, A., Stanier, C., and Pandis, S.: Coupled partitioning, dilution, and chemical aging of semivolatile  
461 organics, *Environ. Sci. Technol.*, 40, 2635-2643, <https://doi.org/10.1021/es052297c>, 2006.
- 462 Donahue, N. M., Epstein, S. A., Pandis, S. N., and Robinson, A. L.: A two-dimensional volatility basis set: 1. organic-aerosol  
463 mixing thermodynamics, *Atmos. Chem. Phys.*, 11, 3303-3318, <https://doi.org/10.5194/acp-11-3303-2011>, 2011.
- 464 Donahue, N. M., Kroll, J. H., Pandis, S. N., and Robinson, A. L.: A two-dimensional volatility basis set – Part 2: Diagnostics  
465 of organic-aerosol evolution, *Atmos. Chem. Phys.*, 12, 615-634, <https://doi.org/10.5194/acp-12-615-2012>, 2012.
- 466 Dong, W., Lin, Y., Wright, J. S., Ming, Y., Xie, Y., Wang, B., Luo, Y., Huang, W., Huang, J., Wang, L., Tian, L., Peng, Y., and  
467 Xu, F.: Summer rainfall over the southwestern Tibetan Plateau controlled by deep convection over the Indian  
468 subcontinent, *Nat. Commun.*, 7, 10925, <https://doi.org/10.1038/ncomms10925>, 2016.
- 469 Duplissy, J., DeCarlo, P. F., Dommen, J., Alfarra, M. R., Metzger, A., Barmpadimos, I., Prevot, A. S. H., Weingartner, E.,  
470 Tritscher, T., Gysel, M., Aiken, A. C., Jimenez, J. L., Canagaratna, M. R., Worsnop, D. R., Collins, D. R., Tomlinson, J.,  
471 and Baltensperger, U.: Relating hygroscopicity and composition of organic aerosol particulate matter, *Atmos. Chem.*



- 472 Phys., 11, 1155-1165, <https://doi.org/10.5194/acp-11-1155-2011>, 2011.
- 473 Einstein, A.: Über die von der molekularkinetischen Theorie der Wärme geforderte Bewegung von in ruhenden Flüssigkeiten  
474 suspendierten Teilchen, 322, 549-560, <https://doi.org/10.1002/andp.19053220806>, 1905.
- 475 Emmons, L. K., Walters, S., Hess, P. G., Lamarque, J. F., Pfister, G. G., Fillmore, D., Granier, C., Guenther, A., Kinnison, D.,  
476 Laepple, T., Orlando, J., Tie, X., Tyndall, G., Wiedinmyer, C., Baughcum, S. L., and Kloster, S.: Description and  
477 evaluation of the model for ozone and related chemical tracers, version 4 (MOZART-4), *Geosci. Model Dev.*, 3, 43-67,  
478 <https://doi.org/10.5194/gmd-3-43-2010>, 2010.
- 479 Epstein, S. A., Riipinen, I., and Donahue, N. M.: A semiempirical correlation between enthalpy of vaporization and  
480 saturation concentration for organic aerosol, *Environ. Sci. Technol.*, 44, 743-748, <https://doi.org/10.1021/es902497z>,  
481 2010.
- 482 Evoy, E., Kamal, S., Patey, G. N., Martin, S. T., and Bertram, A. K.: Unified description of diffusion coefficients from small  
483 to large molecules in organic-water mixtures, *J. Phys. Chem. A*, 124, 2301-2308,  
484 <https://doi.org/10.1021/acs.jpca.9b11271>, 2020.
- 485 Evoy, E., Maclean, A. M., Rovelli, G., Li, Y., Tsimpidi, A. P., Karydis, V. A., Kamal, S., Lelieveld, J., Shiraiwa, M., Reid, J.  
486 P., and Bertram, A. K.: Predictions of diffusion rates of large organic molecules in secondary organic aerosols using the  
487 Stokes-Einstein and fractional Stokes-Einstein relations, *Atmos. Chem. Phys.*, 19, 10073-10085,  
488 <https://doi.org/10.5194/acp-19-10073-2019>, 2019.
- 489 Fast, J. D., Gustafson Jr, W. I., Easter, R. C., Zaveri, R. A., Barnard, J. C., Chapman, E. G., Grell, G. A., and Peckham, S. E.:  
490 Evolution of ozone, particulates, and aerosol direct radiative forcing in the vicinity of Houston using a fully coupled  
491 meteorology-chemistry-aerosol model, *J. Geophys. Res.: Atmos.*, 111, <https://doi.org/10.1029/2005JD006721>, 2006.
- 492 Feng, T., Wang, Y., Hu, W., Zhu, M., Song, W., Chen, W., Sang, Y., Fang, Z., Deng, W., Fang, H., Yu, X., Wu, C., Yuan, B.,  
493 Huang, S., Shao, M., Huang, X., He, L., Lee, Y. R., Huey, L. G., Canonaco, F., Prevot, A. S. H., and Wang, X.: Impact  
494 of aging on the sources, volatility, and viscosity of organic aerosols in Chinese outflows, *Atmos. Chem. Phys.*, 23,  
495 611-636, <https://doi.org/10.5194/acp-23-611-2023>, 2023.
- 496 Fröhlich, R., Cubison, M. J., Slowik, J. G., Bukowiecki, N., Prévôt, A. S. H., Baltensperger, U., Schneider, J., Kimmel, J. R.,  
497 Gonin, M., Rohner, U., Worsnop, D. R., and Jayne, J. T.: The ToF-ACSM: a portable aerosol chemical speciation  
498 monitor with TOFMS detection, *Atmos. Meas. Tech.*, 6, 3225-3241, <https://doi.org/10.5194/amt-6-3225-2013>, 2013.
- 499 Galeazzo, T. and Shiraiwa, M.: Predicting glass transition temperature and melting point of organic compounds via machine  
500 learning and molecular embeddings, *Environ. Sci.: Atmos.*, <https://doi.org/10.1039/D1EA00090J>, 2022.
- 501 Gervasi, N. R., Topping, D. O., and Zuend, A.: A predictive group-contribution model for the viscosity of aqueous organic  
502 aerosol, *Atmos. Chem. Phys.*, 20, 2987-3008, <https://doi.org/10.5194/acp-20-2987-2020>, 2020.
- 503 Gordon, M. and Taylor, J. S.: Ideal copolymers and the second-order transitions of synthetic rubbers. i. non-crystalline  
504 copolymers, *J. Appl. Chem.*, 2, 493-500, <https://doi.org/10.1002/jctb.5010020901>, 1952.
- 505 Grell, G. A., Peckham, S. E., Schmitz, R., McKeen, S. A., Frost, G., Skamarock, W. C., and Eder, B.: Fully coupled "online"  
506 chemistry within the WRF model, *Atmos. Environ.*, 39, 6957-6975, <https://doi.org/10.1016/j.atmosenv.2005.04.027>,  
507 2005.
- 508 Guenther, A. B., Jiang, X., Heald, C. L., Sakulyanontvittaya, T., Duhl, T., Emmons, L. K., and Wang, X.: The Model of  
509 Emissions of Gases and Aerosols from Nature version 2.1 (MEGAN2.1): an extended and updated framework for  
510 modeling biogenic emissions, *Geosci. Model Dev.*, 5, 1471-1492, <https://doi.org/10.5194/gmd-5-1471-2012>, 2012.
- 511 Gunthe, S. S., King, S. M., Rose, D., Chen, Q., Roldin, P., Farmer, D. K., Jimenez, J. L., Artaxo, P., Andreae, M. O., Martin,  
512 S. T., and Pöschl, U.: Cloud condensation nuclei in pristine tropical rainforest air of Amazonia: size-resolved  
513 measurements and modeling of atmospheric aerosol composition and CCN activity, *Atmos. Chem. Phys.*, 9, 7551-7575,  
514 <https://doi.org/10.5194/acp-9-7551-2009>, 2009.
- 515 He, Y., Akherati, A., Nah, T., Ng, N. L., Garofalo, L. A., Farmer, D. K., Shiraiwa, M., Zaveri, R. A., Cappa, C. D., Pierce, J.  
516 R., and Jathar, S. H.: Particle size distribution dynamics can help constrain the phase state of secondary organic aerosol,  
517 *Environ. Sci. Technol.*, 55, 1466-1476, <https://doi.org/10.1021/acs.est.0c05796>, 2021.
- 518 Hu, H.: The distribution of China's population, *Acta Geogr. Sin.*, 2, 33-73, <https://doi.org/10.11821/xb193502002>, 1935.





- 519 Huang, R., Zhang, Z., Huang, G., and Ren, B.: Characteristics of the water vapor transport in east Asian monsoon region and  
520 its differences from that of south Asian monsoon region in summer, *Chinese J. Atmospheric Sci.*, 22, 368-379,  
521 <https://doi.org/10.3878/j.issn.1006-9895.2003.19204>, 1998.
- 522 Huang, Y., Mahrt, F., Xu, S., Shiraiwa, M., Zuend, A., and Bertram, A. K.: Coexistence of three liquid phases in individual  
523 atmospheric aerosol particles, *P. Natl. Acad. Sci. USA*, 118, e2102512118, <https://doi.org/10.1073/pnas.2102512118>,  
524 2021.
- 525 Jathar, S. H., Cappa, C. D., He, Y., Pierce, J. R., Chuang, W., Bilsback, K. R., Seinfeld, J. H., Zaveri, R. A., and Shrivastava,  
526 M.: A computationally efficient model to represent the chemistry, thermodynamics, and microphysics of secondary  
527 organic aerosols (simpleSOM): model development and application to  $\alpha$ -pinene SOA, *Environ. Sci.: Atmos.*, 1, 372-394,  
528 <https://doi.org/10.1039/D1EA00014D>, 2021.
- 529 Jimenez, J. L., Canagaratna, M. R., Donahue, N. M., Prevot, A. S. H., Zhang, Q., Kroll, J. H., DeCarlo, P. F., Allan, J. D.,  
530 Coe, H., Ng, N. L., Aiken, A. C., Docherty, K. S., Ulbrich, I. M., Grieshop, A. P., Robinson, A. L., Duplissy, J., Smith, J.  
531 D., Wilson, K. R., Lanz, V. A., Hueglin, C., Sun, Y. L., Tian, J., Laaksonen, A., Raatikainen, T., Rautiainen, J.,  
532 Vaattovaara, P., Ehn, M., Kulmala, M., Tomlinson, J. M., Collins, D. R., Cubison, M. J., Dunlea, J., Huffman, J. A.,  
533 Onasch, T. B., Alfarra, M. R., Williams, P. I., Bower, K., Kondo, Y., Schneider, J., Drewnick, F., Borrmann, S., Weimer,  
534 S., Demerjian, K., Salcedo, D., Cottrell, L., Griffin, R., Takami, A., Miyoshi, T., Hatakeyama, S., Shimono, A., Sun, J.  
535 Y., Zhang, Y. M., Dzepina, K., Kimmel, J. R., Sueper, D., Jayne, J. T., Herndon, S. C., Trimborn, A. M., Williams, L. R.,  
536 Wood, E. C., Middlebrook, A. M., Kolb, C. E., Baltensperger, U., and Worsnop, D. R.: Evolution of organic aerosols in  
537 the atmosphere, *Science*, 326, 1525, <https://doi.org/10.1126/science.1180353>, 2009.
- 538 Kanakidou, M., Seinfeld, J. H., Pandis, S. N., Barnes, I., Dentener, F. J., Facchini, M. C., Van Dingenen, R., Ervens, B.,  
539 Nenes, A., Nielsen, C. J., Swietlicki, E., Putaud, J. P., Balkanski, Y., Fuzzi, S., Horth, J., Moortgat, G. K., Winterhalter,  
540 R., Myhre, C. E. L., Tsigaridis, K., Vignati, E., Stephanou, E. G., and Wilson, J.: Organic aerosol and global climate  
541 modelling: a review, *Atmos. Chem. Phys.*, 5, 1053-1123, <https://doi.org/10.5194/acp-5-1053-2005>, 2005.
- 542 Karnezi, E., Riipinen, I., and Pandis, S. N.: Measuring the atmospheric organic aerosol volatility distribution: a theoretical  
543 analysis, *Atmos. Meas. Tech.*, 7, 2953-2965, <https://doi.org/10.5194/amt-7-2953-2014>, 2014.
- 544 Kirpes, R. M., Lei, Z., Fraund, M., Gunsch Matthew, J., May Nathaniel, W., Barrett Tate, E., Moffett Claire, E., Schauer  
545 Andrew, J., Alexander, B., Upchurch Lucia, M., China, S., Quinn Patricia, K., Moffet Ryan, C., Laskin, A., Sheesley  
546 Rebecca, J., Pratt Kerri, A., and Ault Andrew, P.: Solid organic-coated ammonium sulfate particles at high relative  
547 humidity in the summertime Arctic atmosphere, *P. Natl. Acad. Sci. USA*, 119, e2104496119,  
548 <https://doi.org/10.1073/pnas.2104496119>, 2022.
- 549 Knopf, D. A. and Alpert, P. A.: Atmospheric ice nucleation, *Nat. Rev. Phys.*, 5, 203-217,  
550 <https://doi.org/10.1038/s42254-023-00570-7>, 2023.
- 551 Knote, C., Hodzic, A., and Jimenez, J. L.: The effect of dry and wet deposition of condensable vapors on secondary organic  
552 aerosols concentrations over the continental US, *Atmos. Chem. Phys.*, 15, 1-18, <https://doi.org/10.5194/acp-15-1-2015>,  
553 2015.
- 554 Kohl, I., Bachmann, L., Hallbrucker, A., Mayer, E., and Loerting, T.: Liquid-like relaxation in hyperquenched water at  $\leq 140$   
555 K, *Phys. Chem. Chem. Phys.*, 7, 3210-3220, <https://doi.org/10.1039/B507651J>, 2005.
- 556 Koop, T., Bookhold, J., Shiraiwa, M., and Pöschl, U.: Glass transition and phase state of organic compounds: dependency on  
557 molecular properties and implications for secondary organic aerosols in the atmosphere, *Phys. Chem. Chem. Phys.*, 13,  
558 19238-19255, <https://doi.org/10.1039/C1CP22617G>, 2011.
- 559 Kuwata, M. and Martin, S. T.: Phase of atmospheric secondary organic material affects its reactivity, *P. Natl. Acad. Sci. USA*,  
560 109, 17354-17359, <https://doi.org/10.1073/pnas.1209071109>, 2012.
- 561 Lane, T. E., Donahue, N. M., and Pandis, S. N.: Simulating secondary organic aerosol formation using the volatility basis-set  
562 approach in a chemical transport model, *Atmos. Environ.*, 42, 7439-7451,  
563 <https://doi.org/10.1016/j.atmosenv.2008.06.026>, 2008a.
- 564 Lane, T. E., Donahue, N. M., and Pandis, S. N.: Effect of NO<sub>x</sub> on secondary organic aerosol concentrations, *Environ. Sci.*  
565 *Technol.*, 42, 6022-6027, <https://doi.org/10.1021/es703225a>, 2008b.



- 566 Li, J., Han, Z., Wu, J., Tao, J., Li, J., Sun, Y., Liang, L., Liang, M., and Wang, Q. g.: Secondary organic aerosol formation  
567 and source contributions over east China in summertime, *Environ. Pollut.*, 306, 119383,  
568 <https://doi.org/10.1016/j.envpol.2022.119383>, 2022.
- 569 Li, M., Zhang, Q., Kurokawa, J. I., Woo, J. H., He, K., Lu, Z., Ohara, T., Song, Y., Streets, D. G., Carmichael, G. R., Cheng,  
570 Y., Hong, C., Huo, H., Jiang, X., Kang, S., Liu, F., Su, H., and Zheng, B.: MIX: a mosaic Asian anthropogenic emission  
571 inventory under the international collaboration framework of the MICS-Asia and HTAP, *Atmos. Chem. Phys.*, 17,  
572 935-963, <https://doi.org/10.5194/acp-17-935-2017>, 2017.
- 573 Li, W., Liu, L., Zhang, J., Xu, L., Wang, Y., Sun, Y., and Shi, Z.: Microscopic evidence for phase separation of organic  
574 species and inorganic salts in fine ambient aerosol particles, *Environ. Sci. Technol.*, 55, 2234-2242,  
575 <https://doi.org/10.1021/acs.est.0c02333>, 2021a.
- 576 Li, Y. and Shiraiwa, M.: Timescales of secondary organic aerosols to reach equilibrium at various temperatures and relative  
577 humidities, *Atmos. Chem. Phys.*, 19, 5959-5971, <https://doi.org/10.5194/acp-19-5959-2019>, 2019.
- 578 Li, Y., An, J., and Gultepe, I.: Effects of additional HONO sources on visibility over the North China Plain, *Adv. Atmos. Sci.*,  
579 31, 1221-1232, <https://doi.org/10.1007/s00376-014-4019-1>, 2014.
- 580 Li, Y., Carlton, A. G., and Shiraiwa, M.: Diurnal and seasonal variations in the phase state of secondary organic aerosol  
581 material over the contiguous US simulated in CMAQ, *ACS Earth Space Chem.*, 5, 1971-1982,  
582 <https://doi.org/10.1021/acsearthspacechem.1c00094>, 2021b.
- 583 Li, Y., Day, D. A., Stark, H., Jimenez, J. L., and Shiraiwa, M.: Predictions of the glass transition temperature and viscosity of  
584 organic aerosols from volatility distributions, *Atmos. Chem. Phys.*, 20, 8103-8122,  
585 <https://doi.org/10.5194/acp-20-8103-2020>, 2020.
- 586 Li, Y., An, J., Min, M., Zhang, W., Wang, F., and Xie, P.: Impacts of HONO sources on the air quality in Beijing, Tianjin and  
587 Hebei Province of China, *Atmos. Environ.*, 45, 4735-4744, <https://doi.org/10.1016/j.atmosenv.2011.04.086>, 2011.
- 588 Li, Y., An, J., Kajino, M., Gultepe, I., Chen, Y., Song, T., and Xin, J.: Impacts of additional HONO sources on O<sub>3</sub> and PM<sub>2.5</sub>  
589 chemical coupling and control strategies in the Beijing–Tianjin–Hebei region of China, *Tellus B*, 67, 23930,  
590 <https://doi.org/10.3402/tellusb.v67.23930>, 2015.
- 591 Li, Z., Xu, W., Zhou, W., Lei, L., Sun, J., You, B., Wang, Z., and Sun, Y.: Insights into the compositional differences of PM<sub>1</sub>  
592 and PM<sub>2.5</sub> from aerosol mass spectrometer measurements in Beijing, China, *Atmos. Environ.*, 301, 119709,  
593 <https://doi.org/10.1016/j.atmosenv.2023.119709>, 2023.
- 594 Lilek, J. and Zuend, A.: A predictive viscosity model for aqueous electrolytes and mixed organic–inorganic aerosol phases,  
595 *Atmos. Chem. Phys.*, 22, 3203-3233, <https://doi.org/10.5194/acp-22-3203-2022>, 2022.
- 596 Liu, P., Li, Y. J., Wang, Y., Bateman, A. P., Zhang, Y., Gong, Z., Bertram, A. K., and Martin, S. T.: Highly viscous states  
597 affect the browning of atmospheric organic particulate matter, *ACS Cent. Sci.*, 4, 207-215,  
598 <https://doi.org/10.1021/acscentsci.7b00452>, 2018.
- 599 Liu, Q., Liu, D., Wu, Y., Bi, K., Gao, W., Tian, P., Zhao, D., Li, S., Yu, C., Tang, G., Wu, Y., Hu, K., Ding, S., Gao, Q., Wang,  
600 F., Kong, S., He, H., Huang, M., and Ding, D.: Reduced volatility of aerosols from surface emissions to the top of the  
601 planetary boundary layer, *Atmos. Chem. Phys.*, 21, 14749-14760, <https://doi.org/10.5194/acp-21-14749-2021>, 2021a.
- 602 Liu, X. and Chen, B.: Climatic warming in the Tibetan Plateau during recent decades, *Int. J. Climatol.*, 20, 1729-1742,  
603 [https://doi.org/10.1002/1097-0088\(20001130\)20:14<1729::AID-JOC556>3.0.CO;2-Y](https://doi.org/10.1002/1097-0088(20001130)20:14<1729::AID-JOC556>3.0.CO;2-Y), 2000.
- 604 Liu, Y., Wu, Z., Wang, Y., Xiao, Y., Gu, F., Zheng, J., Tan, T., Shang, D., Wu, Y., Zeng, L., Hu, M., Bateman, A. P., and  
605 Martin, S. T.: Submicrometer particles are in the liquid state during heavy haze episodes in the urban atmosphere of  
606 Beijing, China, *Environ. Sci. Technol. Lett.*, 4, 427-432, <https://doi.org/10.1021/acs.estlett.7b00352>, 2017.
- 607 Liu, Y., Meng, X., Wu, Z., Huang, D., Wang, H., Chen, J., Chen, J., Zong, T., Fang, X., Tan, T., Zhao, G., Chen, S., Zeng, L.,  
608 Guo, S., Huang, X., He, L., Zeng, L., and Hu, M.: The particle phase state during the biomass burning events, *Sci. Total  
609 Environ.*, 792, 148035, <https://doi.org/10.1016/j.scitotenv.2021.148035>, 2021b.
- 610 Maclean, A. M., Butenhoff, C. L., Grayson, J. W., Barsanti, K., Jimenez, J. L., and Bertram, A. K.: Mixing times of organic  
611 molecules within secondary organic aerosol particles: a global planetary boundary layer perspective, *Atmos. Chem.  
612 Phys.*, 17, 13037-13048, <https://doi.org/10.5194/acp-17-13037-2017>, 2017.



- 613 Maclean, A. M., Li, Y., Crescenzo, G. V., Smith, N. R., Karydis, V. A., Tsimpidi, A. P., Butenhoff, C. L., Faiola, C. L.,  
614 Lelieveld, J., Nizkorodov, S. A., Shiraiwa, M., and Bertram, A. K.: Global distribution of the phase state and mixing  
615 times within secondary organic aerosol particles in the troposphere based on room-temperature viscosity measurements,  
616 *ACS Earth Space Chem.*, 5, 3458-3473, <https://doi.org/10.1021/acsearthspacechem.1c00296>, 2021.
- 617 Marcolli, C. and Krieger, U. K.: Phase changes during hygroscopic cycles of mixed organic/inorganic model systems of  
618 tropospheric aerosols, *J. Phys. Chem. A*, 110, 1881-1893, <https://doi.org/10.1021/jp0556759>, 2006.
- 619 Marshall, F. H., Berkemeier, T., Shiraiwa, M., Nandy, L., Ohm, P. B., Dutcher, C. S., and Reid, J. P.: Influence of particle  
620 viscosity on mass transfer and heterogeneous ozonolysis kinetics in aqueous–sucrose–maleic acid aerosol, *Phys. Chem.*  
621 *Chem. Phys.*, 20, 15560-15573, <https://doi.org/10.1039/C8CP01666F>, 2018.
- 622 Meng, X., Wu, Z., Guo, S., Wang, H., Liu, K., Zong, T., Liu, Y., Zhang, W., Zhang, Z., Chen, S., Zeng, L., Hallquist, M.,  
623 Shuai, S., and Hu, M.: Humidity-dependent phase state of gasoline vehicle emission-related aerosols, *Environ. Sci.*  
624 *Technol.*, 55, 832-841, <https://doi.org/10.1021/acs.est.0c05478>, 2021.
- 625 Miao, R., Chen, Q., Shrivastava, M., Chen, Y., Zhang, L., Hu, J., Zheng, Y., and Liao, K.: Process-based and  
626 observation-constrained SOA simulations in China: the role of semivolatile and intermediate-volatility organic  
627 compounds and OH levels, *Atmos. Chem. Phys.*, 21, 16183-16201, <https://doi.org/10.5194/acp-21-16183-2021>, 2021.
- 628 Mikhailov, E., Vlasenko, S., Martin, S. T., Koop, T., and Pöschl, U.: Amorphous and crystalline aerosol particles interacting  
629 with water vapor: conceptual framework and experimental evidence for restructuring, phase transitions and kinetic  
630 limitations, *Atmos. Chem. Phys.*, 9, 9491-9522, <https://doi.org/10.5194/acp-9-9491-2009>, 2009.
- 631 Murphy, B. N. and Pandis, S. N.: Simulating the formation of semivolatile primary and secondary organic aerosol in a  
632 regional chemical transport model, *Environ. Sci. Technol.*, 43, 4722-4728, <https://doi.org/10.1021/es803168a>, 2009.
- 633 Pankow, J. F.: An absorption model of gas/particle partitioning of organic compounds in the atmosphere, *Atmos. Environ.*, 28,  
634 185-188, [https://doi.org/10.1016/1352-2310\(94\)90093-0](https://doi.org/10.1016/1352-2310(94)90093-0), 1994.
- 635 Petters, M. D. and Kreidenweis, S. M.: A single parameter representation of hygroscopic growth and cloud condensation  
636 nucleus activity, *Atmos. Chem. Phys.*, 7, 1961-1971, <https://doi.org/10.5194/acp-7-1961-2007>, 2007.
- 637 Pöschl, U. and Shiraiwa, M.: Multiphase chemistry at the atmosphere–biosphere interface influencing climate and public  
638 health in the anthropocene, *Chem. Rev.*, 115, 4440-4475, <https://doi.org/10.1021/cr500487s>, 2015.
- 639 Preston, T. C. and Zuend, A.: Equilibration times in viscous and viscoelastic aerosol particles, *Environ. Sci.: Atmos.*,  
640 <https://doi.org/10.1039/D2EA00065B>, 2022.
- 641 Price, H. C., Mattsson, J., and Murray, B. J.: Sucrose diffusion in aqueous solution, *Phys. Chem. Chem. Phys.*, 18,  
642 19207-19216, <https://doi.org/10.1039/C6CP03238A>, 2016.
- 643 Pye, H. O. T., Murphy, B. N., Xu, L., Ng, N. L., Carlton, A. G., Guo, H., Weber, R., Vasilakos, P., Appel, K. W.,  
644 Budisulistiorini, S. H., Surratt, J. D., Nenes, A., Hu, W., Jimenez, J. L., Isaacman-VanWertz, G., Misztal, P. K., and  
645 Goldstein, A. H.: On the implications of aerosol liquid water and phase separation for organic aerosol mass, *Atmos.*  
646 *Chem. Phys.*, 17, 343-369, <https://doi.org/10.5194/acp-17-343-2017>, 2017.
- 647 Qu, Y., Chen, Y., Liu, X., Zhang, J., Guo, Y., and An, J.: Seasonal effects of additional HONO sources and the heterogeneous  
648 reactions of N<sub>2</sub>O<sub>5</sub> on nitrate in the North China Plain, *Sci. Total Environ.*, 690, 97-107,  
649 <https://doi.org/10.1016/j.scitotenv.2019.06.436>, 2019.
- 650 Rasool, Q. Z., Shrivastava, M., Octaviani, M., Zhao, B., Gaudet, B., and Liu, Y.: Modeling volatility-based aerosol phase  
651 state predictions in the Amazon Rainforest, *ACS Earth Space Chem.*, 5, 2910-2924,  
652 <https://doi.org/10.1021/acsearthspacechem.1c00255>, 2021.
- 653 Reid, J. P., Bertram, A. K., Topping, D. O., Laskin, A., Martin, S. T., Petters, M. D., Pope, F. D., and Rovelli, G.: The  
654 viscosity of atmospherically relevant organic particles, *Nat. Commun.*, 9, 956,  
655 <https://doi.org/10.1038/s41467-018-03027-z>, 2018.
- 656 Richards, D. S., Trobaugh, K. L., Hajek-Herrera, J., Price, C. L., Sheldon, C. S., Davies, J. F., and Davis, R. D.: Ion-molecule  
657 interactions enable unexpected phase transitions in organic-inorganic aerosol, *Sci. Adv.*, 6, eabb5643,  
658 <https://doi.org/10.1126/sciadv.abb5643>, 2020.
- 659 Riipinen, I., Pierce, J. R., Donahue, N. M., and Pandis, S. N.: Equilibration time scales of organic aerosol inside



- 660 thermodenuders: Evaporation kinetics versus thermodynamics, *Atmos. Environ.*, 44, 597-607,  
661 <https://doi.org/10.1016/j.atmosenv.2009.11.022>, 2010.
- 662 Roldin, P., Eriksson, A. C., Nordin, E. Z., Hermansson, E., Mogensen, D., Rusanen, A., Boy, M., Swietlicki, E.,  
663 Svenningsson, B., Zelenyuk, A., and Pagels, J.: Modelling non-equilibrium secondary organic aerosol formation and  
664 evaporation with the aerosol dynamics, gas- and particle-phase chemistry kinetic multilayer model ADCHAM, *Atmos.*  
665 *Chem. Phys.*, 14, 7953-7993, <https://doi.org/10.5194/acp-14-7953-2014>, 2014.
- 666 Rothfuss, N. E. and Petters, M. D.: Influence of functional groups on the viscosity of organic aerosol, *Environ. Sci. Technol.*,  
667 51, 271-279, <https://doi.org/10.1021/acs.est.6b04478>, 2017.
- 668 Schervish, M. and Shiraiwa, M.: Impact of phase state and non-ideal mixing on equilibration timescales of secondary organic  
669 aerosol partitioning, *Atmos. Chem. Phys.*, 23, 221-233, <https://doi.org/10.5194/acp-23-221-2023>, 2023.
- 670 Schmedding, R., Rasool, Q. Z., Zhang, Y., Pye, H. O. T., Zhang, H., Chen, Y., Surratt, J. D., Lopez-Hilfiker, F. D., Thornton,  
671 J. A., Goldstein, A. H., and Vizuete, W.: Predicting secondary organic aerosol phase state and viscosity and its effect on  
672 multiphase chemistry in a regional-scale air quality model, *Atmos. Chem. Phys.*, 20, 8201-8225,  
673 <https://doi.org/10.5194/acp-20-8201-2020>, 2020.
- 674 Seinfeld, J. H. and Pandis, S. N.: *Atmospheric chemistry and physics: from air pollution to climate change*, John Wiley &  
675 Sons, 2016.
- 676 Shiraiwa, M. and Seinfeld, J. H.: Equilibration timescale of atmospheric secondary organic aerosol partitioning, *Geophys.*  
677 *Res. Lett.*, 39, <https://doi.org/10.1029/2012GL054008>, 2012.
- 678 Shiraiwa, M., Yee, L. D., Schilling, K. A., Loza, C. L., Craven, J. S., Zuend, A., Ziemann, P. J., and Seinfeld, J. H.: Size  
679 distribution dynamics reveal particle-phase chemistry in organic aerosol formation, *P. Natl. Acad. Sci. USA*, 110, 11746,  
680 <https://doi.org/10.1073/pnas.1307501110>, 2013.
- 681 Shiraiwa, M., Li, Y., Tsimpidi, A. P., Karydis, V. A., Berkemeier, T., Pandis, S. N., Lelieveld, J., Koop, T., and Pöschl, U.:  
682 Global distribution of particle phase state in atmospheric secondary organic aerosols, *Nat. Commun.*, 8, 15002,  
683 <https://doi.org/10.1038/ncomms15002>, 2017.
- 684 Shrivastava, M., Fast, J., Easter, R., Gustafson Jr, W. I., Zaveri, R. A., Jimenez, J. L., Saide, P., and Hodzic, A.: Modeling  
685 organic aerosols in a megacity: comparison of simple and complex representations of the volatility basis set approach,  
686 *Atmos. Chem. Phys.*, 11, 6639-6662, <https://doi.org/10.5194/acp-11-6639-2011>, 2011.
- 687 Shrivastava, M., Rasool, Q. Z., Zhao, B., Octaviani, M., Zaveri, R. A., Zelenyuk, A., Gaudet, B., Liu, Y., Shilling, J. E.,  
688 Schneider, J., Schulz, C., Zöger, M., Martin, S. T., Ye, J., Guenther, A., Souza, R. F., Wendisch, M., and Pöschl, U.:  
689 Tight coupling of surface and in-plant biochemistry and convection governs key fine particulate components over the  
690 Amazon Rainforest, *ACS Earth Space Chem.*, 6, 380-390, <https://doi.org/10.1021/acsearthspacechem.1c00356>, 2022.
- 691 Shrivastava, M., Cappa, C. D., Fan, J., Goldstein, A. H., Guenther, A. B., Jimenez, J. L., Kuang, C., Laskin, A., Martin, S. T.,  
692 Ng, N. L., Petaja, T., Pierce, J. R., Rasch, P. J., Roldin, P., Seinfeld, J. H., Shilling, J., Smith, J. N., Thornton, J. A.,  
693 Volkamer, R., Wang, J., Worsnop, D. R., Zaveri, R. A., Zelenyuk, A., and Zhang, Q.: Recent advances in understanding  
694 secondary organic aerosol: implications for global climate forcing, *Rev. Geophys.*, 55, 509-559,  
695 <https://doi.org/10.1002/2016RG000540>, 2017.
- 696 Song, M., Jeong, R., Kim, D., Qiu, Y., Meng, X., Wu, Z., Zuend, A., Ha, Y., Kim, C., Kim, H., Gaikwad, S., Jang, K.-S., Lee,  
697 J. Y., and Ahn, J.: Comparison of phase states of PM<sub>2.5</sub> over megacities, Seoul and Beijing, and their implications on  
698 particle size distribution, *Environ. Sci. Technol.*, <https://doi.org/10.1021/acs.est.2c06377>, 2022.
- 699 Song, Y. C., Haddrell, A. E., Bzdek, B. R., Reid, J. P., Bannan, T., Topping, D. O., Percival, C., and Cai, C.: Measurements  
700 and predictions of binary component aerosol particle viscosity, *J. Phys. Chem. A*, 120, 8123-8137,  
701 <https://doi.org/10.1021/acs.jpca.6b07835>, 2016.
- 702 Stark, H., Yatavelli, R. L. N., Thompson, S. L., Kang, H., Krechmer, J. E., Kimmel, J. R., Palm, B. B., Hu, W., Hayes, P. L.,  
703 Day, D. A., Campuzano-Jost, P., Canagaratna, M. R., Jayne, J. T., Worsnop, D. R., and Jimenez, J. L.: Impact of thermal  
704 decomposition on thermal desorption instruments: advantage of thermogram analysis for quantifying volatility  
705 distributions of organic species, *Environ. Sci. Technol.*, 51, 8491-8500, <https://doi.org/10.1021/acs.est.7b00160>, 2017.
- 706 Tan, W., Li, C., Liu, Y., Meng, X., Wu, Z., Kang, L., and Zhu, T.: Potential of polarization lidar to profile the urban aerosol



- 707 phase state during haze episodes, *Environ. Sci. Technol. Lett.*, 7, 54-59, <https://doi.org/10.1021/acs.estlett.9b00695>,  
708 2020.
- 709 Tong, Y.-K., Liu, Y., Meng, X., Wang, J., Zhao, D., Wu, Z., and Ye, A.: Relative humidity-dependent viscosity of single quasi  
710 aerosol particle and possible implications for atmospheric aerosol chemistry, *Phys. Chem. Chem. Phys.*,  
711 <https://doi.org/10.1039/D2CP00740A>, 2022.
- 712 Wu, Z. J., Poulain, L., Henning, S., Dieckmann, K., Birmili, W., Merkel, M., van Pinxteren, D., Spindler, G., Müller, K.,  
713 Stratmann, F., Herrmann, H., and Wiedensohler, A.: Relating particle hygroscopicity and CCN activity to chemical  
714 composition during the HCCT-2010 field campaign, *Atmos. Chem. Phys.*, 13, 7983-7996,  
715 <https://doi.org/10.5194/acp-13-7983-2013>, 2013.
- 716 Xu, W., Chen, C., Qiu, Y., Li, Y., Zhang, Z., Karnezi, E., Pandis, S. N., Xie, C., Li, Z., Sun, J., Ma, N., Xu, W., Fu, P., Wang,  
717 Z., Zhu, J., Worsnop, D. R., Ng, N. L., and Sun, Y.: Organic aerosol volatility and viscosity in the North China Plain:  
718 contrast between summer and winter, *Atmos. Chem. Phys.*, 21, 5463-5476, <https://doi.org/10.5194/acp-21-5463-2021>,  
719 2021.
- 720 Xu, W., Xie, C., Karnezi, E., Zhang, Q., Wang, J., Pandis, S. N., Ge, X., Zhang, J., An, J., Wang, Q., Zhao, J., Du, W., Qiu, Y.,  
721 Zhou, W., He, Y., Li, Y., Li, J., Fu, P., Wang, Z., Worsnop, D. R., and Sun, Y.: Summertime aerosol volatility  
722 measurements in Beijing, China, *Atmos. Chem. Phys.*, 19, 10205-10216, <https://doi.org/10.5194/acp-19-10205-2019>,  
723 2019.
- 724 Zaveri, R. A., Easter, R. C., Fast, J. D., and Peters, L. K.: Model for Simulating Aerosol Interactions and Chemistry  
725 (MOSAIC), *J. Geophys. Res.: Atmos.*, 113, <https://doi.org/10.1029/2007JD008782>, 2008.
- 726 Zaveri, R. A., Easter, R. C., Shilling, J. E., and Seinfeld, J. H.: Modeling kinetic partitioning of secondary organic aerosol  
727 and size distribution dynamics: representing effects of volatility, phase state, and particle-phase reaction, *Atmos. Chem.*  
728 *Phys.*, 14, 5153-5181, <https://doi.org/10.5194/acp-14-5153-2014>, 2014.
- 729 Zaveri, R. A., Shilling, J. E., Zelenyuk, A., Zawadowicz, M. A., Suski, K., China, S., Bell, D. M., Veghte, D., and Laskin, A.:  
730 Particle-phase diffusion modulates partitioning of semivolatile organic compounds to aged secondary organic aerosol,  
731 *Environ. Sci. Technol.*, 54, 2595-2605, <https://doi.org/10.1021/acs.est.9b05514>, 2020.
- 732 Zaveri, R. A., Shilling, J. E., Zelenyuk, A., Liu, J., Bell, D. M., D'Ambro, E. L., Gaston, C. J., Thornton, J. A., Laskin, A.,  
733 Lin, P., Wilson, J., Easter, R. C., Wang, J., Bertram, A. K., Martin, S. T., Seinfeld, J. H., and Worsnop, D. R.: Growth  
734 kinetics and size distribution dynamics of viscous secondary organic aerosol, *Environ. Sci. Technol.*, 52, 1191-1199,  
735 <https://doi.org/10.1021/acs.est.7b04623>, 2018.
- 736 Zeng, P., Sun, F., Liu, Y., Wang, Y., Li, G., and Che, Y.: Mapping future droughts under global warming across China: a  
737 combined multi-timescale meteorological drought index and SOM-Kmeans approach, *Weather Clim. Extreme*, 31,  
738 100304, <https://doi.org/10.1016/j.wace.2021.100304>, 2021.
- 739 Zhang, J., Lian, C., Wang, W., Ge, M., Guo, Y., Ran, H., Zhang, Y., Zheng, F., Fan, X., Yan, C., Daellenbach, K. R., Liu, Y.,  
740 Kulmala, M., and An, J.: Amplified role of potential HONO sources in O<sub>3</sub> formation in North China Plain during  
741 autumn haze aggravating processes, *Atmos. Chem. Phys.*, 22, 3275-3302, <https://doi.org/10.5194/acp-22-3275-2022>,  
742 2022.
- 743 Zhang, Y., Chen, Y., Lei, Z., Olson, N. E., Riva, M., Koss, A. R., Zhang, Z., Gold, A., Jayne, J. T., Worsnop, D. R., Onasch, T.  
744 B., Kroll, J. H., Turpin, B. J., Ault, A. P., and Surratt, J. D.: Joint impacts of acidity and viscosity on the formation of  
745 secondary organic aerosol from isoprene epoxydiols (IEPOX) in phase separated particles, *ACS Earth Space Chem.*, 3,  
746 2646-2658, <https://doi.org/10.1021/acsearthspacechem.9b00209>, 2019a.
- 747 Zhang, Y., Nichman, L., Spencer, P., Jung, J. I., Lee, A., Heffernan, B. K., Gold, A., Zhang, Z., Chen, Y., Canagaratna, M. R.,  
748 Jayne, J. T., Worsnop, D. R., Onasch, T. B., Surratt, J. D., Chandler, D., Davidovits, P., and Kolb, C. E.: The cooling  
749 rate- and volatility-dependent glass-forming properties of organic aerosols measured by broadband dielectric  
750 spectroscopy, *Environ. Sci. Technol.*, 53, 12366-12378, <https://doi.org/10.1021/acs.est.9b03317>, 2019b.
- 751 Zheng, B., Tong, D., Li, M., Liu, F., Hong, C., Geng, G., Li, H., Li, X., Peng, L., Qi, J., Yan, L., Zhang, Y., Zhao, H., Zheng,  
752 Y., He, K., and Zhang, Q.: Trends in China's anthropogenic emissions since 2010 as the consequence of clean air actions,  
753 *Atmos. Chem. Phys.*, 18, 14095-14111, <https://doi.org/10.5194/acp-18-14095-2018>, 2018.



754 Ziemann, P. J. and Atkinson, R.: Kinetics, products, and mechanisms of secondary organic aerosol formation, Chem. Soc.

755 Rev., 41, 6582-6605, <https://doi.org/10.1039/C2CS35122F>, 2012.

756

757

758

759

760

761

762

763

764

765

766

767

768

769

770

771

772

773

774

775

776

777

778

779

780

781

782

783

784

785



786 **Table 1.** Sensitivity calculations for evaluating the effects of simulated SOA volatility distributions (sensitivity case A), RH (sensitivity  
787 case B) and the water absorbed by inorganic components (sensitivity case C) on viscosity estimations.

788

Cases	$C^*$ at 298 K and $\Delta H_{\text{vap}}$ in each volatility bin	The liquid water content considered in viscosity estimations	RH
Base case	0.1, 1, 10, 100, and 1000 $\mu\text{g m}^{-3}$ with $\Delta H_{\text{vap}}$ of 142, 131, 120, 109, and 98 $\text{kJ mol}^{-1}$	water absorbed by SOA particles with the assumption that SOA particles are externally mixed with inorganics	RH simulated by WRF-Chem
Sensitivity case A	0.0001, 1, 10, 100, and 1000 $\mu\text{g m}^{-3}$ with $\Delta H_{\text{vap}}$ of 40, 131, 120, 109, and 98 $\text{kJ mol}^{-1}$	water absorbed by SOA particles with the assumption that SOA particles are externally mixed with inorganics	RH simulated by WRF-Chem
Sensitivity case B	0.1, 1, 10, 100, and 1000 $\mu\text{g m}^{-3}$ with $\Delta H_{\text{vap}}$ of 142, 131, 120, 109, and 98 $\text{kJ mol}^{-1}$	water absorbed by SOA particles with the assumption that SOA particles are externally mixed with inorganics	RH simulated by WRF-Chem increased by a factor of 10%
Sensitivity case C	0.1, 1, 10, 100, and 1000 $\mu\text{g m}^{-3}$ with $\Delta H_{\text{vap}}$ of 142, 131, 120, 109, and 98 $\text{kJ mol}^{-1}$	water absorbed by both SOA particles and inorganic components with the assumption that SOA particles are internally mixed with inorganics	RH simulated by WRF-Chem

789

790

791

792

793

794

795

796

797

798

799

800

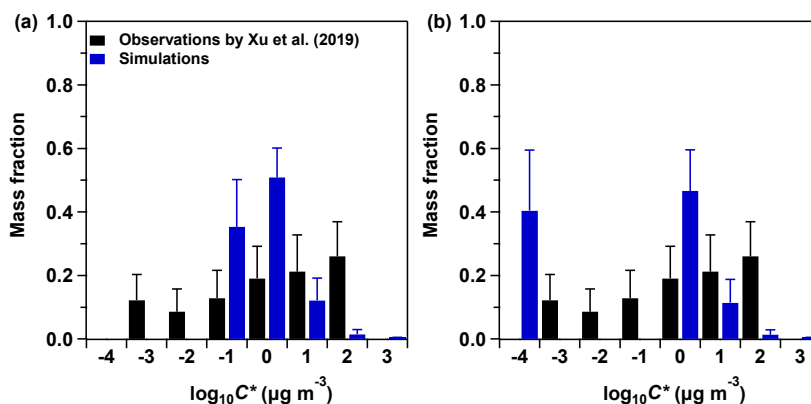
801

802

803

804

805



806

807 **Figure 1.** Comparison of the average volatility distributions of observed OOA and simulated SOA at the IAP site during 20 May – 23 June

808 2018. The black bars represent the volatility distributions of observed OOA adopted from Xu et al. (2019). The blue bars represent the

809 volatility distributions of SOA simulated by WRF-Chem, with five  $C^*$  bins set to be 0.1, 1, 10, 100, and 1000  $\mu\text{g m}^{-3}$  at 298 K in (a), and

810 0.0001, 1, 10, 100, and 1000  $\mu\text{g m}^{-3}$  at 298 K in (b). The blue error bars represent the one standard deviation.

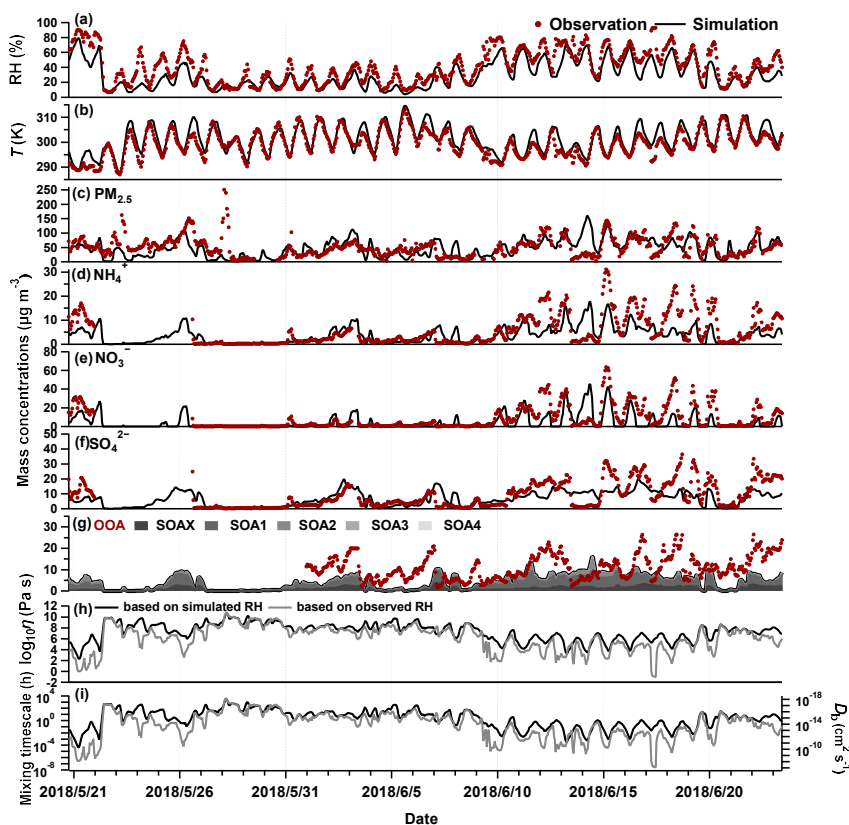
811

812

813

814





815

816 **Figure 2.** Observations and simulations of temporal variations of (a) RH, (b) *T*, (c) PM<sub>2.5</sub> concentrations, (d) NH<sub>4</sub><sup>+</sup> concentrations, (e)  
 817 NO<sub>3</sub><sup>-</sup> concentrations, and (f) SO<sub>4</sub><sup>2-</sup> concentrations at the IAP site. (g) Observed OOA concentrations (red dots) and simulated SOA  
 818 concentrations, with SOAX, SOA1, SOA2, SOA3, and SOA4 represent the SOA with *C*<sup>\*</sup> of 0.1, 1, 10, 100, and 1000 µg m<sup>-3</sup> at 298 K,  
 819 respectively. (h) SOA viscosity, and (i) bulk diffusion coefficients and mixing timescale of organic molecules within 200 nm SOA particles  
 820 calculated using the RH simulated by the WRF-Chem model or the RH observed at the IAP site.

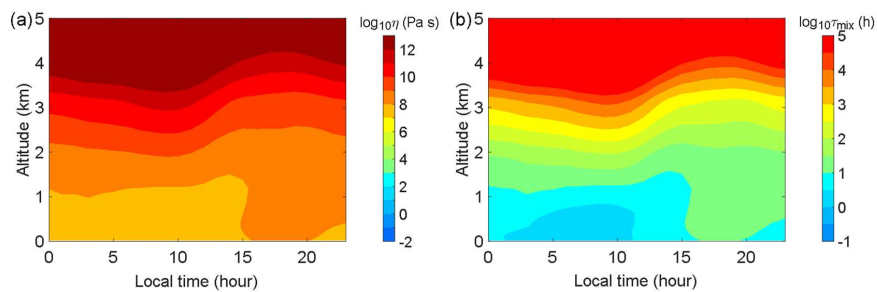
821

822

823

824

825



826

827 **Figure 3.** Median diurnal and vertical profiles of estimated (a) SOA viscosity and (b) mixing timescales for organic molecules within 200  
828 nm SOA particles at the IAP site during May 20 – June 23 in 2018. Note: altitude is approximate and estimated from WRF pressure layers.

829

830

831

832

833

834

835

836

837

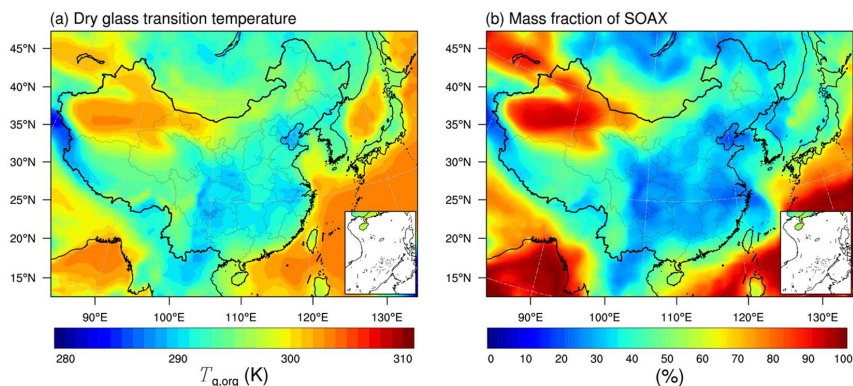
838

839

840

841

842



843

844

**Figure 4.** The predicted median surface values of (a) glass transition temperature of SOA particles at the dry condition and (b) mass fractions of SOAX ( $C^* = 0.1 \mu\text{g m}^{-3}$  at 298 K) during May 20 – June 23 in 2018 simulated in the base case (Table 1).

845

846

847

848

849

850

851

852

853

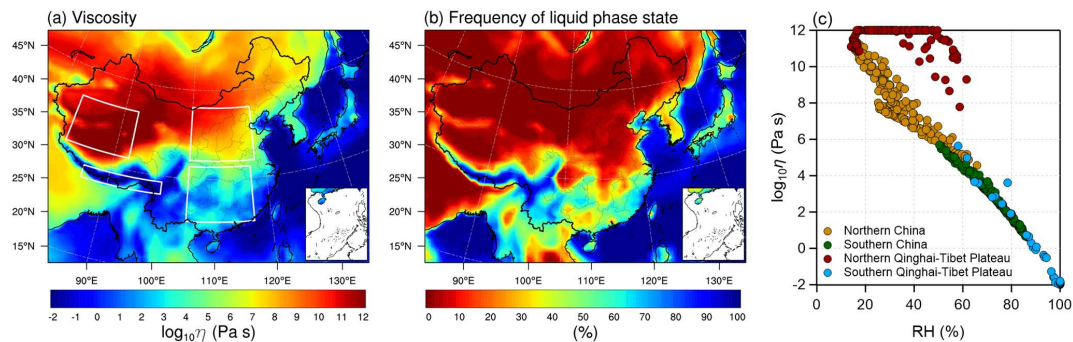
854

855

856

857

858



859  
860 **Figure 5.** WRF-Chem predicted (a) median surface values of viscosity and (b) the percent time that an organic aerosol particle is in the  
861 liquid phase state during May 20 – June 23 in 2018. (c) The median values of viscosity as a function of RH calculated for selected regions  
862 in the northern China, southern China, northern Qinghai-Tibet Plateau, and southern Qinghai-Tibet Plateau as specified by white boxes in  
863 panel (a).

864

865

866

867

868

869

870

871

872

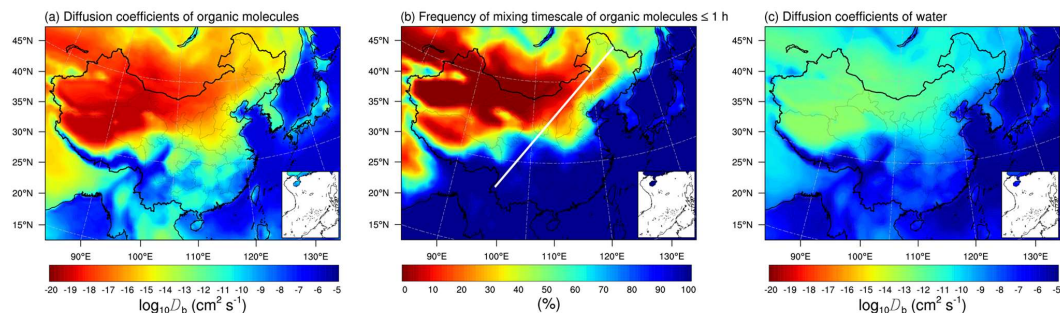
873

874

875

876

877



878

879 **Figure 6.** WRF-Chem predicted median surface values of the diffusion coefficients of (a) organic molecules and (c) water molecules in  
880 SOA particles. (b) The percent time that the mixing timescale of organic molecules in a 200 nm particle is less than 1 h during May 20 –  
881 June 23 in 2018. The white line indicates the “Hu Huanyong Line” (Hu, 1935).

882

883

884

885

886

887

888

889

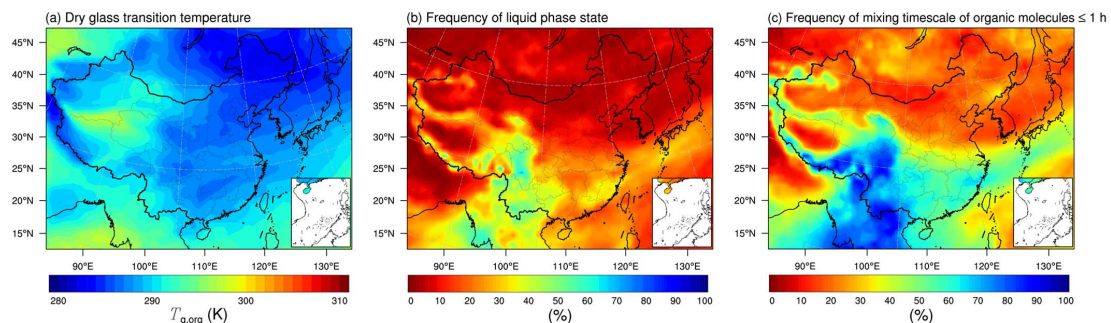
890

891

892

893

894



895

896 **Figure 7.** WRF-Chem predicted median values of (a) glass transition temperature of SOA particles at the dry condition, (b) the percent  
897 time that an organic aerosol particle is in the liquid phase state, and (c) the percent time that the mixing timescale of organic molecules in a  
898 200 nm particle is less than 1 h at 500 hPa during May 20 – June 23 in 2018.

899

900

901

902

903

904

905

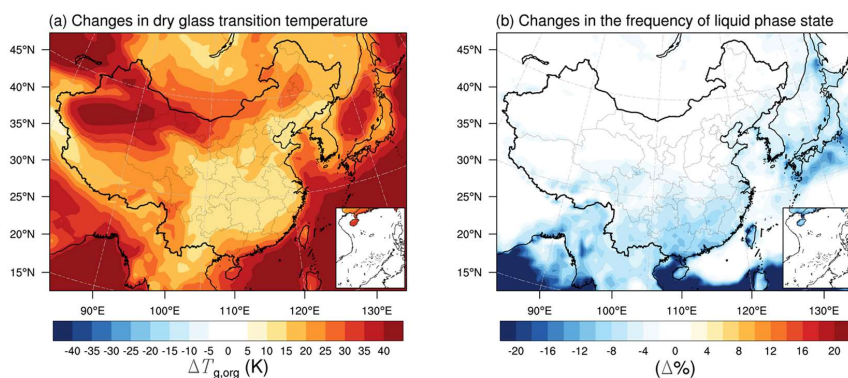
906

907

908

909

910



911

912 **Figure 8.** Modelled median differences of (a) glass transition temperature of SOA particles at the dry condition, and (b) the percent time  
913 that an organic aerosol particle is in the liquid phase state between a sensitivity case with the lowest  $C^*$  of  $0.0001 \mu\text{g m}^{-3}$  at 298 K ( $\Delta H_{\text{vap}}$  of  
914  $40 \text{ kJ mol}^{-1}$ , case A in Table 1) and a base case with the lowest  $C^*$  of  $0.1 \mu\text{g m}^{-3}$  at 298 K ( $\Delta H_{\text{vap}}$  of  $142 \text{ kJ mol}^{-1}$ , Table 1).

915

916

917

918

919

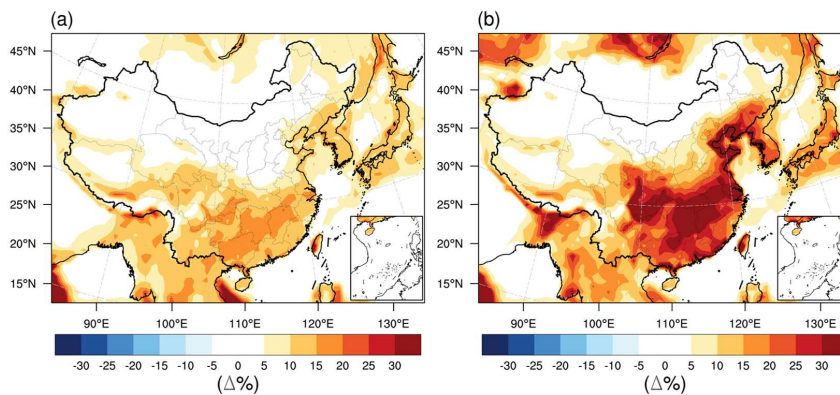
920

921

922

923

924



925

926

**Figure 9.** (a) Impacts of RH on the percent time that an organic aerosol particle is in the liquid phase state: modelled median differences

927

between a case with the WRF-Chem simulated RH increased by a factor of 10 % (case B, Table 1) and a base case (Table 1) with the

928

WRF-Chem simulated RH. (b) Impacts of the water absorbed by inorganics on the percent time that an organic aerosol particle is in the

929

liquid phase state: modelled median differences between a case considering the water absorbed by both SOA particles and inorganics (case

930

C, Table 1) and a base case (Table 1) considering the water absorbed by SOA particles solely.

931